IVYSPRING INTERNATIONAL PUBLISHER

International Journal of Biological Sciences

2027; 23(1): 507-527. doi: 10.7150/ijbs.137518

Research Paper

A Novel Engineered Peptide Disrupting Lactate Dehydrogenase A Function: Potentiation by *Salmonella* Precision Delivery for Cancer Therapy

Jun Kwon*, Amal Senevirathne*, Muhammad Bakhsh, John Hwa Lee✉

College of Veterinary Medicine, Jeonbuk National University, 79 Gobong-ro, Iksan, 54596, Jeollabuk-do, Republic of Korea.

* These authors contributed equally to this work.

✉ Corresponding author: E-mail: johnhlee@jbnu.ac.kr, Tel: +82-63-850-0940.

© 2027 The Author(s). This is an open access article distributed under the Creative Commons Attribution 4.0 International Licence, subject to the Publisher's Terms of Use at https://ivyspring.com/terms.

Received: 2026.05.09; Accepted: 2026.10.27; Published: 2027.01.01

Abstract

Metabolic reprogramming is a hallmark of cancer, with lactate dehydrogenase A (LDHA) driving the Warburg effect and supporting uncontrolled growth, immune evasion, and resistance to therapy. In this study, we introduce a reverse-engineering strategy to disable LDHA via targeted protein aggregation. Computational analyses using the TANGO algorithm identified conserved aggregation-prone regions (APRs) across mouse LDHA isoforms. Tandem repeat peptides linked by flexible spacers were designed to disrupt LDHA's quaternary structure, promoting misfolding and aggregation rather than active-site inhibition. Among the designed candidates, Pept#2 demonstrated the strongest anticancer activity, selectively inducing apoptosis, oxidative stress, and migration suppression in cancer cell lines. Mechanistically, Pept#2 impaired compensatory glycolytic responses during mitochondrial stress, reduced lactate production, depleted intracellular ATP levels, and directly suppressed LDHA enzymatic activity. Electron microscopy and aggregation kinetics further supported peptide-mediated LDHA aggregation and loss of soluble protein fractions. For *in vivo* applications, Pept#2 was encoded in a eukaryotic expression plasmid and delivered via an attenuated *Salmonella* vector (JOL2500 carrying pcDNA3.2::Pept#2), enabling localized tumor expression. This combined strategy significantly reduced tumor growth and metastatic burden in CT26 and 4T1 murine tumor models, accompanied by extensive histopathological tumor disruption and pro-inflammatory cytokine induction, without substantial off-target toxicity. Collectively, these findings highlight LDHA aggregation as a novel therapeutic avenue and demonstrate the potential of integrating structure-guided peptide design with bacterial delivery systems for precise metabolic cancer therapies.

Keywords: LDHA aggregation; peptide therapeutics; metabolic cancer therapy; *Salmonella*-mediated delivery; Warburg effect

Introduction

Cancer remains a leading cause of mortality worldwide [1], driving continuous efforts to develop novel and innovative therapeutic modalities that can overcome the limitations of conventional treatments, such as chemotherapy, radiotherapy, and small-molecule targeted treatment agents [2]. The hallmark of cancer is profound metabolic reprogramming, particularly the preferential use of aerobic glycolysis, a phenomenon known as the Warburg effect. Glucose is readily metabolized into lactate, irrespective of the presence or absence of oxygen in the surrounding intracellular environment [3, 4]. This metabolic shift sustains rapid cellular proliferation and biomass accumulation, fosters metastatic potential, and establishes an immunosuppressive tumor that leads to cancer progression and resistance to therapy [2, 5]. Lactate dehydrogenase A (LDHA) is a key enzyme in the glycolytic pathway. This tetrameric enzyme catalyzes the conversion of pyruvate to lactate, with the concomitant regeneration of NAD^+ [6, 7]. It maintains glycolytic flux, thereby meeting the heightened anabolic and energetic demands for tumor cell proliferation and metastasis [5]. Elevated LDHA expression is a hallmark of diverse human

malignancies, including breast, gastric, pancreatic, and hepatocellular carcinomas, and its upregulation is often driven by oncogenic transcription factors, such as c-Myc and hypoxia-inducible factor 1 (HIF-1), which correlate with disease aggressiveness and poor prognosis [8]. Inhibition of LDHA disrupts these metabolic circuits, resulting in an energy crisis, increased oxidative stress, cell cycle arrest, and induction of apoptosis in tumor cells [2, 4, 5]. Hence, LDHA is a plausible target for therapeutic interventions as it plays a prominent role in cancer cells, which are distinctly different from normal healthy cells.

The suppression of LDHA is strongly associated with cancer regression due to its significant role in cancer metabolism. To date, small-molecule inhibitors capable of interacting with active or allosteric sites of LDHA, impeding substrate or cofactor binding, have demonstrated promise in therapeutic applications. However, during clinical translation, some small molecules demonstrate off-target effects, impeding their application in human treatments [9]. A fundamental aspect of cancer treatment is specificity, which should distinguish healthy cells from cancer cells; hence, for LDHA inhibition, it is imperative to develop more specific strategies than those currently available.

In recent years, human amyloids have introduced the concept of protein deposits or aggregates associated with diseases and other functional aspects within various tissues [10]. A key discovery was made related to Alzheimer's disease, where the disease-associated amyloid beta (Aβ) could interact with glycoproteins of the herpes virus [11]. This process results in protein entrapment of viral particles, leading to amyloid-mediated antiviral function [12]. The association of Aβ with the herpes virus was driven by a process later recognized as aggregation-prone region-targeted protein interaction, where the specialized homologous region of Aβ interacts with the glycoproteins (beta sheet stacking), leading to functional alterations of protein-protein interactions. It is now possible to apply bioinformatics tools (e.g., TANGO algorithm) to predict protein regions with greater precision and accuracy, thereby stimulating the aggregation of target proteins [13].

As a novel strategy to interfere with LDHA function in cancer cells, we employed a peptide-based agent with several distinct advantages, including high specificity, tunable pharmacological properties, low intrinsic toxicity, and amenability to further modifications. Plausible sequence elements were selected using bioinformatic predictions. To enhance peptide efficacy, LDHA isoforms 1 and 2 were selected for *in silico* analysis, and peptide candidates were evaluated based on specificity and predicted efficacy. Peptides predicted to target both LDHA isoforms effectively were selected for synthesis and downstream analysis. By leveraging earlier practical efficacies of aggregation-prone regions (APRs), the selected sequences were designed as duplicate sequences connected by a flexible connector intended to interfere with the critical structural domains of LDHA, potentially disrupting quaternary assembly and proper assembly and destabilizing the enzyme's active quaternary structure. This may induce aggregation and misfolding, thereby abrogating LDHA's catalytic activity. The present approach is conceptually distinct from classical competitive inhibition, providing a novel avenue to functionally incapacitate key enzymes involved in oncogenic processes that are refractory to conventional interventions, such as small-molecule therapies. Modern computational approaches enable precise prediction and simulation of peptides that interact with specific domains within the three-dimensional structure of proteins. Concerning LDHA tetramerization interfaces, the N-terminal arm has exhibited the capacity to disrupt the association of LDHA subunits [5].

Owing to the critical role of LDHA in cancer cell metabolism, its functional disruption can induce ATP depletion, increase reactive oxygen species (ROS) generation, and promote mitochondrial apoptosis, thereby suppressing cancer progression and biomass accumulation [14]. To translate the current conceptual framework into a practical reality under *in vivo* conditions, we cloned the open reading frames of the peptide into a commercial eukaryotic plasmid vector and investigated its ability to induce cancer apoptosis in multiple cell lines, revealing that Pept#2 has a higher potential to induce apoptosis. The next challenge is the delivery of therapeutic plasmid vectors into *in vivo* conditions; thus, we utilized an attenuated *Salmonella* strain specifically designed for plasmid delivery. Ideally, the utilization of *Salmonella* in the current LDHA interference approach is appealing, as *Salmonella* also competes for the same energy reserves within cancer cells [15]. Furthermore, peptide sequences are highly specific; hence, the risk of off-target effects is minimal. Furthermore, as a living being, *Salmonella* also competes for resources in the tumor microenvironment. Therefore, the effects of ATP starvation may be significant in cancer cells infected with pathogen-delivered therapeutic peptides.

This study describes the first attempt to suppress LDHA function in cancer cells by employing specialized APR peptides and provides preclinical evidence to evaluate their potential. Building on the

convergence of structural elucidation, peptide engineering, and cancer metabolism research, this study elaborates the rationale, design methodology, mechanistic underpinnings, and antitumor potential of LDHA aggregation as a promising frontier in metabolic cancer therapy.

Results

Peptide design and identification of aggregation-prone regions

In silico identification of APRs in mouse LDHA isoforms 1 and 2 was conducted with the TANGO algorithm [16]. The analyses were performed in physiological conditions (pH 7.4, 298 K, ionic strength 0.02 M) to predict segments with high probability of β-sheet aggregation [17]. To select high-performance sequences, the TANGO pipeline categorized candidate segments into three primary predictive modes (fewer false positives; high stringency, best overall performance; balanced sensitivity/specificity, and high sensitivity; broadest capture) (Table S2). We identified some of the high-scoring APR segments, with typically 5-15 residues, with high potential to stack β-sheet and cross-β spine formation. Four peptides were selected according to high aggregation scores, sequence conservation within LDHA isoforms and good physicochemical characteristics (Table S2). To optimize those sequences for cellular applications, the peptides were constructed as double tandem repeats to enhance interaction potential [18]. Furthermore, charged aspartic acid residues were added to limit self-folding, and a tryptophan residue was added to ensure accurate concentration measurements using absorbance [19]. The final sequences are listed in Table S3. The structural design is shown in Figure 1A.

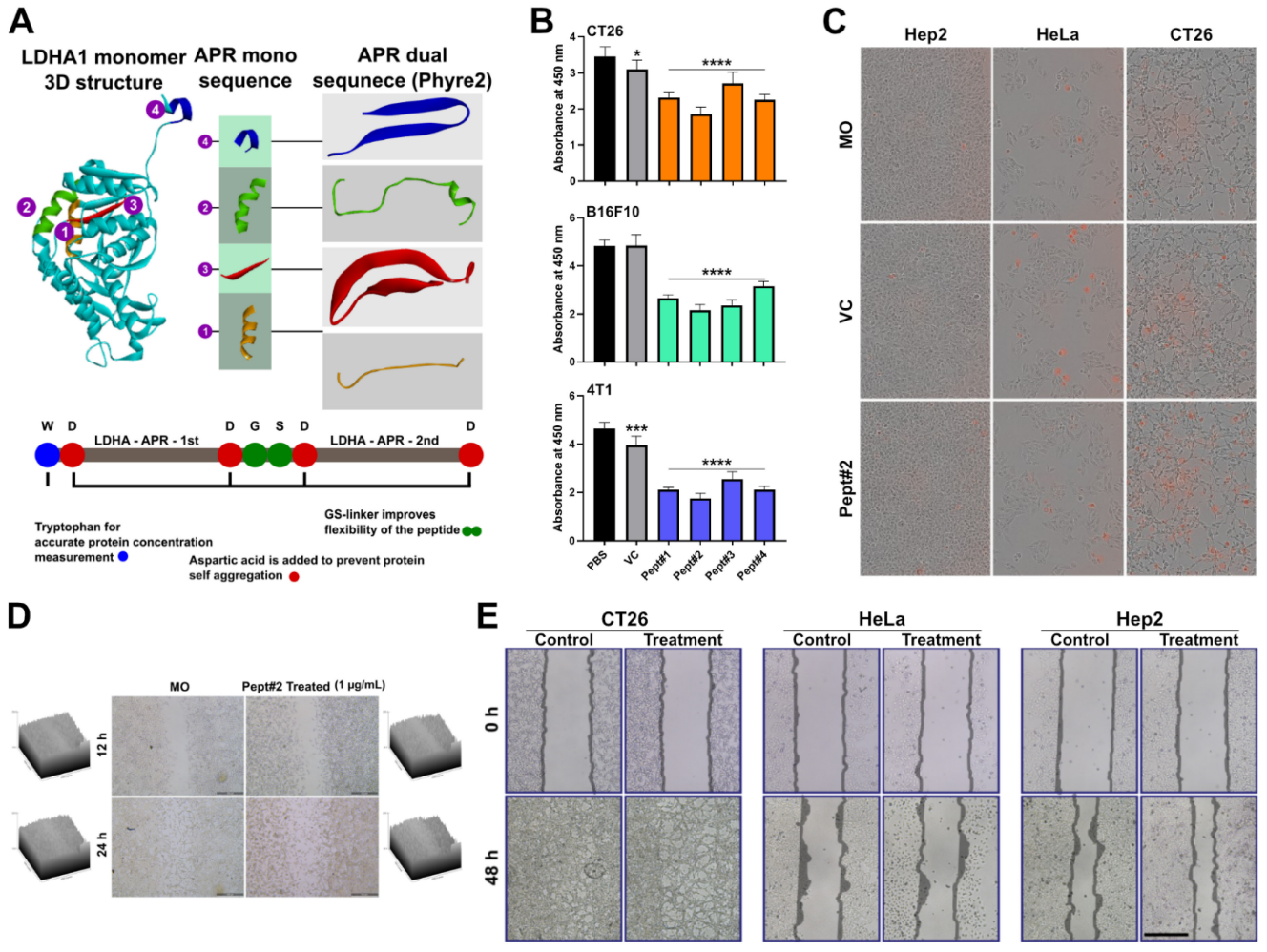

Figure 1. Schematic representation of APR peptide design and preliminary assessment. (A) The graphical representation of the distribution of selected APRs in the LDHA molecule. The amino acid architecture of peptides used in the study. (B) Peptide anti-cancer activity and specificity assessment. Peptide-induced cytotoxicity was evaluated upon *in vitro* transfection. Cellular effect was compared using CT26, B16F10, and 4T1 cancer cell lines. (C) The functional specificity was evaluated by assessing apoptosis induction using murine cell lines (CT26) and human cell lines (Hep2 and HeLa). Observations were recorded using IncuCyte live imaging system. (D) Assessment of peptide effect on cancer metastasis. The time-dependent effect on wound healing is demonstrated. (E) Peptide's functional specificity on wound healing. Wound healing assay used CT26 (target cells) and human cancer cell lines. HeLa and Hep2. Gap closure assessment demonstrates a profound effect of Pept#2 on CT26, but not on human cell lines. Differences were considered significant if the $p < 0.05$. The asterisks represent the significant difference between the treated and PBS control.

Physicochemical properties of deduced peptides

The physicochemical properties of the four selected peptide candidates were estimated by using the *in silico* tool PepCalc [20]. The peptide lengths were determined to be 21, 33, 29 and 25 amino acid residues for Pept#1, Pept#2, Pept#3 and Pept#4. Among these, Pept#2 has a net charge of zero at physiological pH (7.00), which is known as a favorable factor for aggregate nucleation [21]. Furthermore, Pept#2 demonstrated lower estimated solubility compared to the other peptide candidates, which indicates that Pept#2 is more likely to be nucleated efficiently. LDHA, being a soluble enzyme, could be important in reducing solubility to induce protein aggregation during protein-peptide interaction [22]. Furthermore, amino acid residues such as proline are known to kink structures when repeated, especially near hydrophobic stretches.

Cloning and confirmation

The selected peptide sequences were cloned into the pcDNA3.2 eukaryotic expression vector (3.4 kb). Insertion was confirmed by PCR and restriction enzyme digestion, followed by plasmid propagation and extraction. For *in vivo* delivery, the constructs were transformed into the attenuated *Salmonella* strain JOL2500, a vector previously characterized for efficient host-cell invasion and cytosolic plasmid release [23]. The constructed strains were designated as JOL2500 VC (JOL2500 carrying empty pcDNA3.2) and JOL2500 Pept#2 (JOL2500 carrying the pcDNA3.2::Pept#2).

Anticancer efficacy of peptide constructs

The initial assessment of the four selected peptides was conducted on transfection-induced cytotoxicity in the CT26, B16F10 and 4T1 murine cancer cell lines. Compared to the vector control (VC) and media-only cell lines, all four peptides reduced cancer cell viability significantly (Fig. 1B). Of the four peptides, Pept#2 showed the highest cell viability reduction of all cell lines, probably due to its physicochemical properties which favor aggregate formation (Table S4). To evaluate the specificity of the peptides, we compared the effect of Pept#2 on the murine cell line CT26 and human cell lines Hep2 and HeLa, to investigate species-specificity of Pept#2. Cytotoxicity was monitored with the IncuCyte imaging system, and propidium iodide (PI) was used as a marker for late apoptosis. Our results showed a significant increase in apoptosis induction in the mouse CT26 cells, and no significant effect was observed on the human Hep2 and HeLa lines (Fig. 1C and Fig. S1).

The effect of anti-cancer peptide on cancer migration and specificity

The effect of Pept#2 on cancer cell proliferation was evaluated with a wound healing assay. Initially, the time-dependent effects of Pept#2 on cancer cell migration was checked in CT26 cells, transfected with Pept#2 carrying plasmid, over 36 hours. The gap closure was observed prominently at 24 and 36 hours post-transfection (Fig. 1D). To compare migration inhibition levels between target and non-target cells, transfected CT26 and HeLa/Hep2 cell lines were studied over 48 hours. In the Pept#2-transfected CT26 cells, gap closure was significantly inhibited, and the wound area was largely unclosed compared to the untreated control (Fig. 1E). In contrast, Pept#2 plasmid transfection did not affect wound closure in HeLa and Hep2 cells. The migration patterns of both human cell lines were similar in the control and treated cells. These results suggest that Pept#2 has a selective inhibitory effect on the migration of murine CT26 cells.

Anti-cancer effect of pure synthetic peptide

To characterize the intrinsic activity of the peptide, purified Pept#2 was prepared, and its solubility was optimized by the combination of DMSO (6%), heat and pH adjustments. Before assay, the cell internalization of Pept#2 was explored using immunofluorescence assay and dose-dependent increase in cellular uptake was confirmed (Fig. S2). The cytotoxic activity of the pure peptide was tested in the murine (4T1 and CT26) and human (Hep2 and HeLa) cancer cell lines at a concentration gradient of 0-5 µg/well. The cell viability levels were found to be lower for the murine target cell lines than for the human non-target cell lines (Fig. 2A). To investigated whether enhanced cytosolic accumulation could amplify its therapeutic efficacy of Pept#2, chitosan nanoparticle encapsulation was employed. In order to further investigate the mechanism of action, we monitored apoptosis in 4T1 cells by using Annexin V/PI staining on chitosan nanoparticles to stain the cell. Chitosan-encapsulated Pept#2 treatments led to a much higher percentage of apoptotic cells than chitosan nanoparticles alone (Fig. 2B-C). To determine if this increase was related to oxidative stress, cells were stained and analyzed with H2DCF-DA. The oxidative stress was significantly higher in chitosan-encapsulated Pept#2 groups (Fig. 2D-E). While chitosan nanoparticles alone contributed to baseline apoptotic responses, the significant increase observed in the chitosan-encapsulated Pept#2 group confirms the additive therapeutic potency of the peptide payload. This suggests that the peptide drives the cytotoxic response beyond the baseline effect of the nanoparticle carrier.

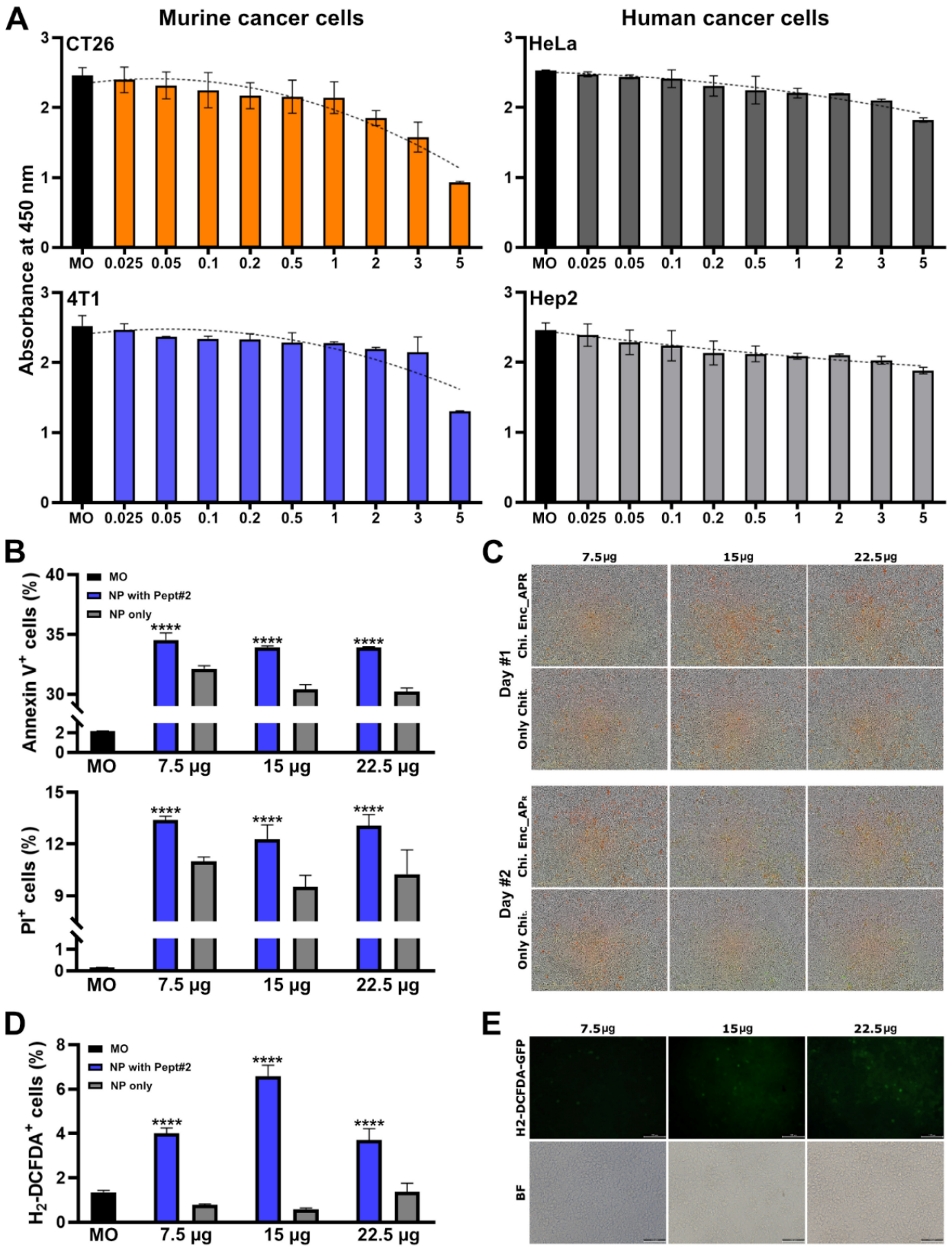

Figure 2. Synthesized APR Pept#2 activity characterization. (A) The assessment of concentration-dependent cytotoxic responses of Pept#2 on target cell lines, mouse cancer 4T1 and CT26 cells, and non-target cell lines, human cancer cell lines Hep2 and HeLa. The trendline indicates the direction and the level of response of each cell line to increasing concentration of Pept#2. (B) Flow cytometry for assessment of chitosan nanoparticle encapsuled Pept#2 induced cellular apoptosis using Annexin V/PI assay. (C) The Annexin V/PI-stained cell live images obtained after exposure to chitosan encapsuled Pept#2. (D) Flow cytometry analysis of oxidative response induction in chitosan encapsulated Pept#2 treated cells using H_2-DCFDA assay. (E) Fluorescence microscopy images obtained during H_2-DCFDA assay. Differences were considered significant if the $p < 0.05$. The asterisks represent the significant difference between the treated and MO alone control.

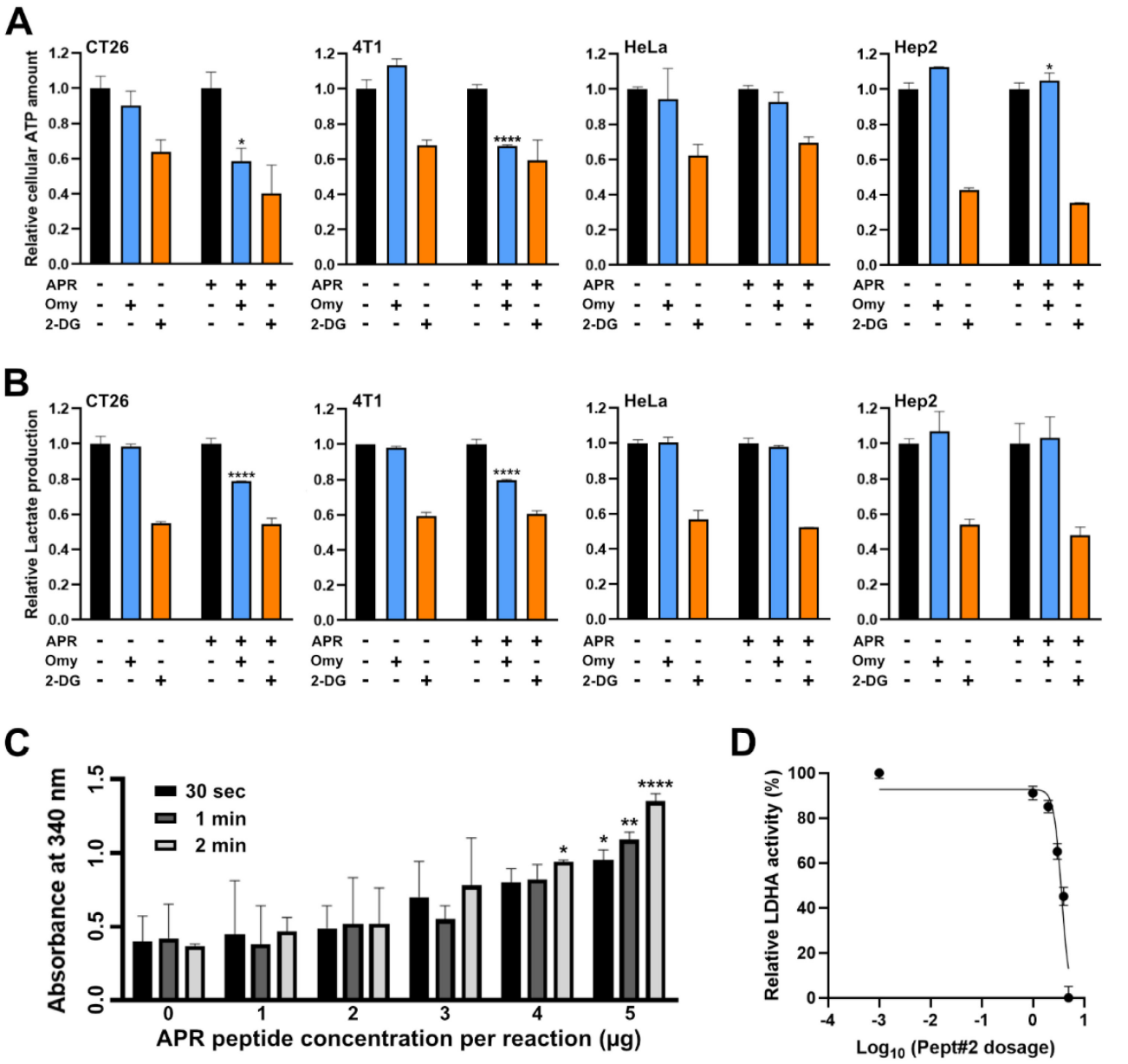

Figure 3. Biochemical assessment of LDHA functional suppression. (A) The assessment of intracellular ATP production under Pept#2, oligomycin (Omy) and 2-Deoxy-D-glucose (2-DG) exposures. (B) The relative lactate production under Pept#2, Omy, and 2-DG exposures. The asterisks represent the significant difference between the Pept#2 exposed and non-exposed groups. (C) Absorbance-based assessment of NADH utilization function to evaluate LDHA suppression in the presence of APR Pept#2. The reaction controls were kept as LDHA alone and increasing concentrations of Pept#2 (1-5 μg), co-incubated with a constant concentration of LDHA. The concentration-dependent suppression is demonstrated with the standard deviation. Dose-dependent inhibition of LDHA activity by Pept#2. The data were fitted using a non-linear regression analysis (four-parameter logistic model) to calculate the IC_{50} value (3.6 μg/reaction). Error bars represent the SD of three independent replicates. Relative LDHA activity was normalized to the 0 μg control (100%). The asterisks represent the significant difference between the same colored LDHA only groups.

Biochemical assessment of LDHA functional suppression

The specificity of LDHA inhibition under mitochondrial stress is evaluated in oligomycin and 2-deoxy-D-glucose (2-DG) response (Fig. 3A–B). In human cells, oligomycin-treated cells showed a compensatory increase in glycolytic flux in response to mitochondrial stress as shown in Fig. 3A–B. However, Pept#2-treated murine cells failed to initiate this compensatory shift towards glycolysis and exhibited reduced lactate production. Furthermore, ATP levels were significantly lower and the total cellular ATP levels were also lower with oligomycin stress (Fig. 3A–B).

To confirm direct inhibition of LDHA, we monitored the enzymatic activity of recombinant LDHA in the presence of Pept#2 by measuring oxidation of NADH (340 nm). Pept#2 treatment inhibited LDHA enzymatic activity significantly compared to the LDHA only control (Fig. 3C). The inhibition was both concentration and time dependent

and was more pronounced in the higher levels of Pept#2 (Fig. 3C). This result further demonstrates that Pept#2 is able to directly inhibit the catalytic activity of LDHA *in vitro*. In addition, nonlinear regression of relative LDHA activity with respect to logarithmic Pept#2 concentration showed a sigmoidal dose-dependent inhibitory activity (Fig. 3D). Based on a four-parameter logistic curve fit, we found that the half-maximal inhibitory concentration (IC_{50}) of Pept#2 was 3.6 µg/reaction.

Pept#2 interaction with LDHA isoforms

To investigate the potential of Pept#2 to interact with LDHA protein, we conducted a docking analysis using the ZDock server. The result identified high-scoring interaction poses between Pept#2 and LDHA monomers (Fig. S3). These data suggest that Pept#2 is likely to bind to LDHA subunits, thereby potentially disrupting the assembly of functional LDHA tetramers.

Structural modeling of Pept#2 interaction with mouse and human LDHA

To better understand the structure of the peptide interaction as well as species-selective behavior, the molecular docking with mouse and human LDHA was performed using the HDOCK server (Fig. S7, Table S5). We found that the 13-mer APR motif is highly conserved between mouse (aa 112-124; RNVNIFKFIIPNI) and human LDHA (112-124; RNVNIFKFIIPNV), sharing 92.3% sequence identity with only one I124V substitution (Fig. S7A). The docking analysis showed that Pept#2 binds to the two orthologs differently. In mouse LDHA, Pept#2 had direct, high-affinity interactions with the N-terminal tetramerization arm (Gln20 at 3.22 Å and Asn21 at 2.36 Å) and with the inter-subunit assembly residues Lys90 (1.67 Å) and Gln297/Asn298 (2.25-2.72 Å) (Fig. S7B, Table S5). As the N-terminal arm is responsible for stabilizing the active LDHA tetramer, this binding mode is the structural mechanism for peptide-induced quaternary disruption and aggregation. On the other hand, docking to human LDHA involved a peripheral surface containing residues 118-127 and the C-terminal helix (residues 324-332) which did not interact with the N-terminal tetramerization arm or the inter-subunit interface (Fig. S7B). The results indicate that Pept#2 selectively works on the quaternary assembly machinery of mouse LDHA and is responsible for its selective suppression in cancer cells in murine mice.

Combined effect of *Salmonella* and Pept#2

To evaluate the cumulative effect of *Salmonella*-mediated peptide delivery on cancer cells, 4T1 cells were treated with either the JOL2500 VC or the JOL2500 Pept#2. Flow cytometry analysis and oxidative stress assays revealed significantly higher levels of apoptosis and oxidative stress in cells treated with the Pept#2-expressing *Salmonella* compared to the vector control (Fig. 4). These findings indicate that the delivery of Pept#2 by *Salmonella* enhances the cytotoxic response in 4T1 cells.

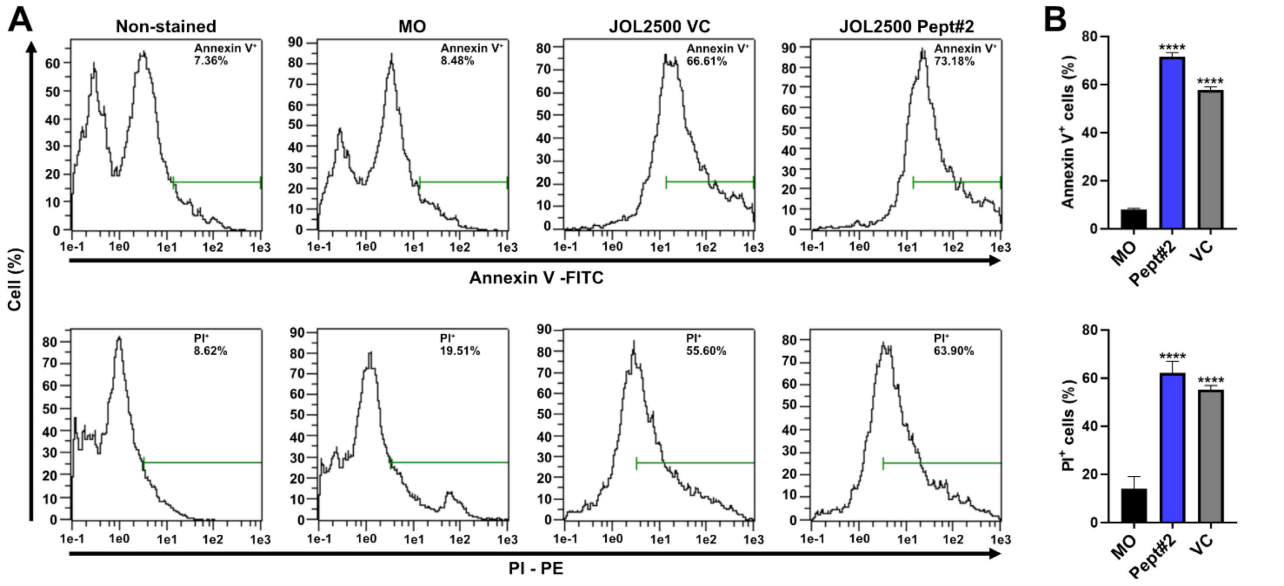

Figure 4. Combined effect of *Salmonella* and Pept#2 on cancer cell apoptosis and cytotoxicity. (A) The flow cytometry analysis after bactofection with JOL2500 carrying empty pcDNA3.2 (JOL2500 VC) and JOL2500 carrying the pcDNA3.2::Pept#2 (JOL2500 Pept#2). (B) Bar diagram representing quantified Annexin V or PI positive cells. Significance level was determined at $p < 0.05$ against the MO control.

Hemolytic safety and biocompatibility of Pept#2

The hemolytic potential of pure Pept#2 was evaluated using a standard sheep blood hemolysis assay. After 1 hour of incubation at 37 °C, significant hemolysis was not observed across the tested peptide concentrations (1–5 µg). At the highest concentration, hemolytic activity remained well below the 5% threshold established for biological safety (Fig. S4) [24]. Furthermore, the biological compatibility of the peptide was assessed *in silico* using ProtParam, PeptideRanker, ToxinPred, and HemoPI. The results of these analyses indicated no harmful predictions for biological applications, supporting the suitability of the peptide for experimental use.

Electron microscopy observation of protein aggregates

The induced protein aggregates are insoluble and tend to precipitate in the solution. TEM images at 100,000 × magnification revealed the presence of precipitation in the PBS and APR Pept#2 specimens (Fig. 5A). However, Pept#2 interaction with the LDHA-purified protein induced distinct dark spots, visualized by negative uranyl acetate staining. The size of most of the particles ranged between 20 and 40 nm and the 3D plots demonstrate the surface roughness, indicating that LDHA potentially precipitated upon interaction with Pept#2.

The effect of an anti-cancer peptide on cellular acidification

To determine the effect of Pept#2 on the LDHA-mediated conversion of pyruvate to lactate, we evaluated the impact on cellular acidification using the pH-sensitive dye BCECF-AM. CT26 cells were treated with serial Pept#2 concentration (0-20 µg/well) and the intracellular acidity was quantified according to fluorescence intensity. The highest decrease in intracellular acidity was observed at 2 µg of Pept#2 (Fig. 5B). At much higher concentrations of Pept#2, the inhibitory effect is reduced, meaning that a stoichiometric ratio between the target protein and the peptide is needed to suppress the functional responses of the target protein (Fig. 5B).

Assessment of aggregation kinetics

Protein aggregation kinetics were monitored via absorbance scans between 280 and 460 nm. The peptide-induced aggregation effect was maximal at a 2µg concentration and decreased as the concentration increased to 10 µg. While peak absorption occurred between 280 and 300 nm, absorbance between 300 and 400 nm served as a direct indicator of aggregate formation (Fig. 5C). Aggregates formed rapidly, within 2–5 minutes, and remained stable throughout the 120-minute incubation period (Fig. 5C). Concurrently, absorbance at 280 nm showed a time-dependent decrease in the soluble protein fraction during co-incubation with the APR peptide, confirming a shift from a soluble to an aggregated state (Fig. 5D).

The peptide effect on metastatic 4T1 cells

Therapeutic potential of JOL2500 Pept#2 was evaluated in 4T1 metastatic breast cancer model. The treatment was administrated one week after tumor implantation and followed by two booster shots at one-week intervals. At the end of the study, tumors and spleens were aseptically retrieved. The mice treated with JOL2500 Pept#2 showed significantly less tumor mass and splenomegaly than the control group (Fig. 6A–C).

Long-term metastatic burden was assessed in the visceral organs and intestinal tissue by macroscopical and histopathological analysis (Fig. 6D). The PBS and JOL2500 VC groups showed metastatic lesion in lung and focal tumor infiltration in liver. In contrast, Pept#2-treated mice demonstrated clean tissue profiles. Especially, Pept#2 treated mice showed significantly reduced tumoral nodule compared to PBS and JOL2500 VC groups, indicating that this treatment was successful in reducing metastatic progression.

In vivo tumor reduction using CT26 ectopic tumors

To evaluate the therapeutic efficacy of *Salmonella*-delivered Pept#2, CT26 tumor-bearing mice were treated at the tumor volume of around 100 mm^3. At the endpoint of the study, mice treated with JOL2500 Pept#2 had significantly reduced tumor mass compared to the PBS and VC group (Fig. 7A–B). Notably, excised tumors from the Pept#2-treated group exhibited internal fluid-filled cavities and necrotic cores. These structural changes, which were absent in control tumors, account for the observed discrepancy between the recorded tumor volumes and the final tumor masses, as further confirmed by histopathological analysis (Fig. 8).

To test the effect of *Salmonella* on short-term metastasis, mice were injected with Fluo-4 AM-stained CT26 cells after the *Salmonella* treatment. Flow cytometry of the lungs, the primary metastasis organ, demonstrated a significant reduction in the number of Fluo-4 AM positive cells in mice treated with the JOL2500 Pept#2 compared to the control (Fig. 7C–D). The results demonstrate the *Salmonella*-based delivery of Pept#2 inhibits the development of primary tumors and cancer cells spreading to metastatic sites.

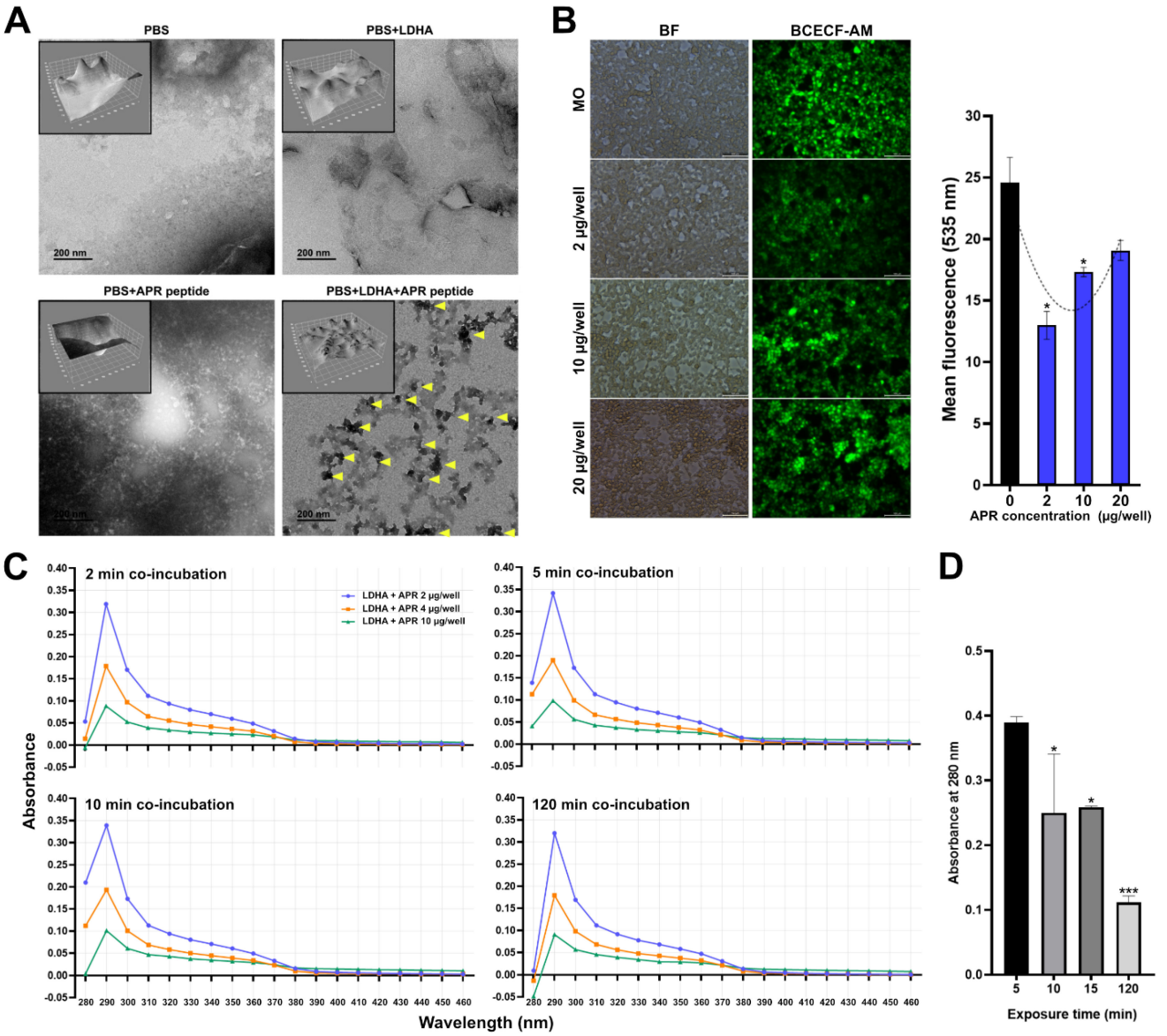

Figure 5. Evaluation of the LDHA protein aggregation kinetics. (A) Transmission electron microscopy image of protein aggregates. Sub images depict the surface 3D plots. The yellow arrows indicate protein aggregates that appeared as dark spherical entities in the visual span. (B) APR Pept#2 effect on cell acidification trends. The BCECF-AM assay was conducted to compare CT26 cell acidification upon various concentrated APR Pept#2 treatment (2, 10, and 20 μg/well). After six hours of treatment, cells were stained with BCECF-AM and observed under the fluorescent microscope and fluorescent intensity was quantified. Significance level was determined at $p < 0.05$ against the MO control. (C) Absorbance scan upon aggregation. Changes of absorbance during protein aggregation were measured for varying APR Pept#2 concentrations using pure peptide and measured at varying time intervals, 2, 5, 10, and 120 min. (D) The variation in the soluble protein fraction. The variation in soluble protein fraction was estimated by measuring absorbance at 280 nm over 0-, 10-, 20-, and 120-minute intervals. Significance level was determined at $p < 0.05$ against the MO control. The asterisks represent the significant difference against LDHA only group.

Histopathological examination of tumor tissues

Tumor histopathology for CT26 and 4T1 tumors revealed the morphological differences in the treated and control groups (Fig. 8A–B). In the untreated and VC groups, tumor tissues displayed densely packed cells which show still intact structure but minimal necrotic regions in CT26 and vacuolization in 4T1 tissue. In contrast, tumors infected with JOL2500 Pept#2 had a marked change in structure. CT26 tumor tissues showed increased stromal spacing, cellular degeneration, nuclear pyknosis, and widespread necrotic zones. Similarly, 4T1 tumors demonstrated severe necrosis, cellular shrinkage, and vacuolization. These histological alterations, including the loss of cellular cohesion and increased acellular areas, were consistent in both murine tumors, confirming the systemic cytotoxic activity of the Pept#2 application.

Evaluation of intact LDHA in tumor tissue using immunohistochemistry

To evaluate the effect of *Salmonella*-delivered Pept#2 on LDHA protein levels *in situ*, we performed

immunohistochemical (IHC) analysis on excised tumor sections. In both CT26 and 4T1 models, the PBS-treated groups exhibited strong, diffuse DAB staining, indicating high levels of intact LDHA throughout the tumor tissue (Fig. 8A–B). The JOL2500 VC groups showed some non-immunostained regions associated with *Salmonella*-induced necrosis; however, the overall LDHA expression remained comparable to the PBS control. In contrast, tumors treated with JOL2500 Pept#2 showed a marked reduction in LDHA-positive staining across the tumor. Notably, LDHA expression was preserved only at the tumor margins, where proliferative and migratory tumor cells are typically concentrated. The IHC result also provides a clue that APR peptide was expressed within tumor cells successfully and induced the peptide-mediated LDHA degradation.

To provide definitive biochemical evidence of LDHA degradation by APR treatment, dot blot assay was performed using purified LDHA co-incubated with Pept#2 peptides (Supplementary Fig. S6). The result showed a dose-dependent reduction in the intact LDHA detection, validating that Pept#2 directly interacts with and promote LDHA degradation. The evidence also reflects that the application of the therapeutic strain is attributable to the loss of LDHA signal in tumors.

Cytokine responses by qRT-PCR

The intratumoral cytokine expression was studied with RT-qPCR to assess the inflammatory response following treatment. The tumors treated with *Salmonella* showed the trends that are more likely to express pro-inflammatory markers TNF-α, IFN-γ and IL-6 than those treated with the control (Fig. 8C–D). In contrast, the anti-inflammatory marker IL-4 was reduced in the JOL2500 Pept#2-treated tumor. These changes in cytokine expression indicate that *Salmonella* vehicle itself can promote an intratumoral pro-inflammatory environment.

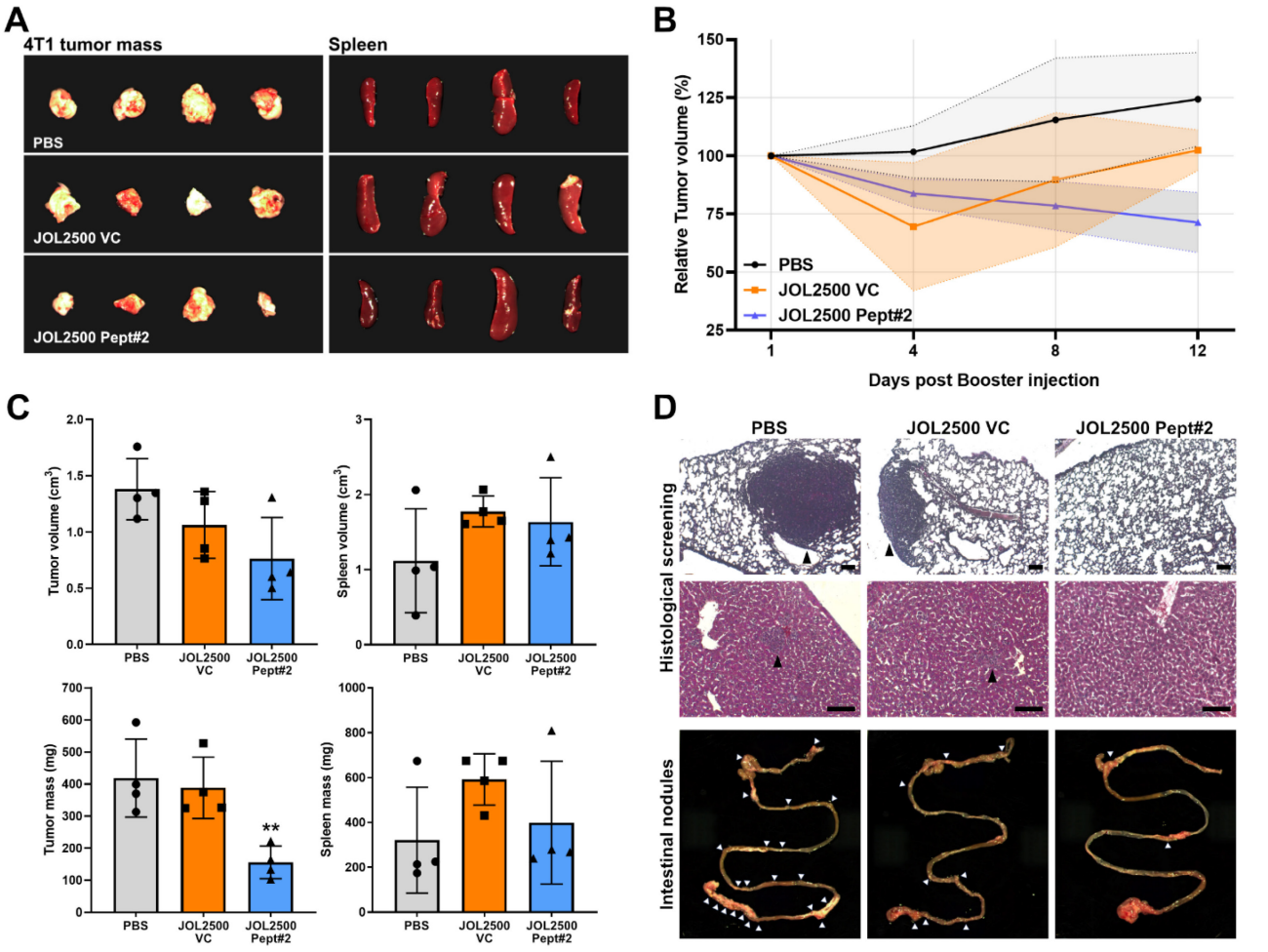

Figure 6. *In vivo* treatment effect of therapeutic strain on 4T1 metastatic tumors. (A) Gross images of excised tumor masses and spleens from 4T1 tumor-bearing BALB/c mice treated with PBS (control), JOL2500 VC, or JOL2500 Pept#2. The therapeutic strain, JOL2500 Pept#2, treatment led to visibly reduced tumor and spleen size compared to controls. (B) Tumor volume changes upon treatment. (C) Tumor reduction in 4T1 tumor mice and splenic inflammation. Quantitative analysis of tumor and spleen parameters: Tumor area (cm^2), tumor mass (mg), spleen area (cm^2), and spleen mass (mg) were measured at the endpoint. The asterisks represent the significant difference against PBS control. (D) *In vivo* long-term metastasis inhibition effect evaluation. Histological screening was performed using lungs and livers (Scale bar = 100 μm). PBS and JOL2500 VC treated mice showed tumoral nodules in tissues (black arrowheads). In quantification of intestinal nodules, the white color arrowheads indicate the observable nodules formed by metastatic cancer.

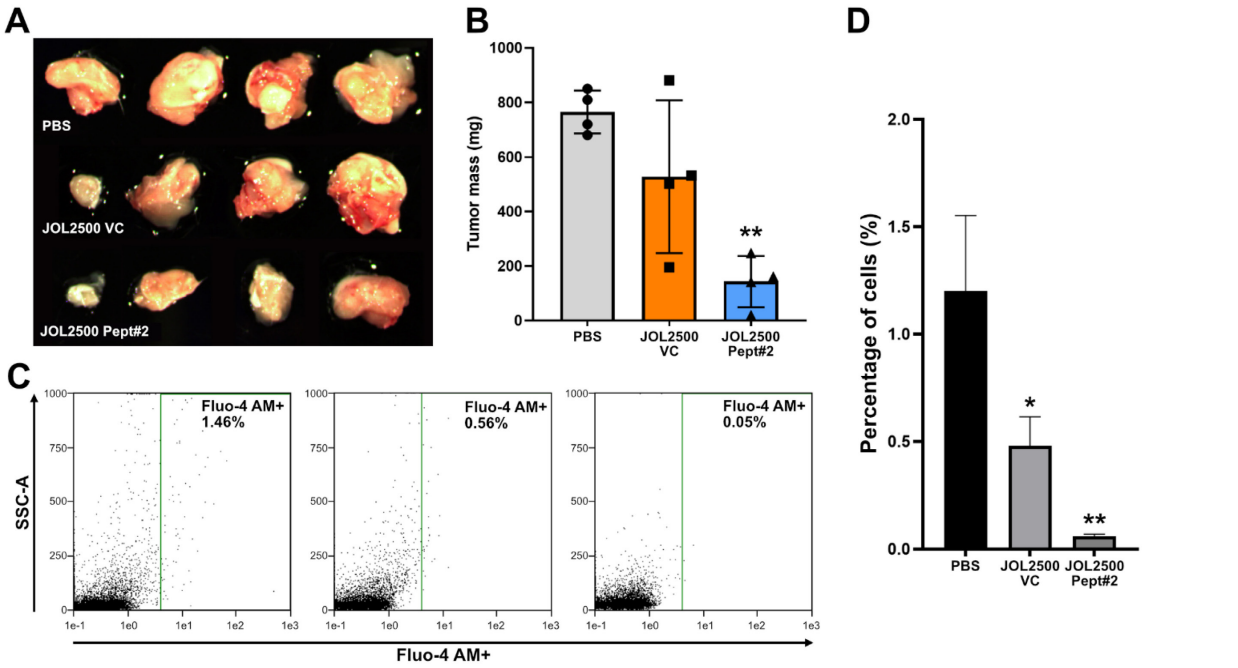

Figure 7. *In vivo* therapeutic efficacy of therapeutic strain, JOL2500 Pept#2, in CT26 tumor models. (A) Gross images of excised tumor masses and spleens from CT26 tumor implanted mice treated with PBS, JOL2500 VC, or JOL2500 Pept#2. (B) Quantitative analysis of tumor mass at the endpoint. (C-D) Effects of *Salmonella* therapeutics in *in vivo* short-term metastasis model. (C) Representative flow cytometry plots indicating Fluo-4AM positive cells in lung tissues. (D) Bar diagram of quantified Fluo-4AM positive cells. Significance level was determined at $p < 0.05$ against the PBS control.

Discussion

A hallmark of cancer cells is their reliance on aerobic glycolysis for energy and materials. This process, known as the Warburg effect, supports rapid proliferation, redox homeostasis, and adaptation to the hypoxic tumor microenvironments (TME) [25]. LDHA plays a central role in this metabolic reprogramming by catalyzing the conversion of pyruvate to lactate while regenerating NAD^+, thereby sustaining high glycolytic flux. Elevated LDHA expression has been correlated with tumor aggressiveness, immune evasion, therapy resistance, and poor prognosis across multiple cancer types. Consequently, LDHA has emerged as an attractive therapeutic target; however, direct enzymatic inhibition using small molecules faces challenges related to specificity, systemic toxicity, and compensatory metabolic rewiring [4, 26-28]. It has also been noted that LDHA overexpression in solid tumors correlates with aggressive phenotypes, resistance to apoptosis, and poor clinical outcomes (Fig. S5) [29, 30]. In this context, our study introduced a fundamentally different strategy: functional inactivation of LDHA through aggregation-inducing APR peptides delivered intracellularly via a tumor-targeting *Salmonella* vector [31-33].

Established small-molecule LDHA inhibitors often exhibit limited clinical efficacy due to their poor selectivity and off-target effects [34]. Alternatively, LDHA-homologous peptide sequences offer enhanced interaction specificity, supporting highly specific intermolecular interactions that promote self-aggregation and functional inactivation of tetrameric LDHA. This strategy exploits transiently exposed structural vulnerabilities in dynamic protein states, selectively impairing LDHA-driven cancer metabolism. Based on prior antiviral APR studies that demonstrated enhanced efficacy with tandem repeats, the peptides were designed as dual-repeat sequences (Fig. 1A) [18]. Charged aspartic acid residues and a flexible linker were incorporated to maintain spatial accessibility and limit self-folding. However, the *in vivo* application is restricted by rapid renal clearance, non-tumor specificity and poor cell penetration [35]. To overcome these limitations, bioengineered *Salmonella* vehicle, JOL2500, was utilized for tumor-tropic delivery. The *Salmonella* platform selectively colonizes the hypoxic nutrient-rich TME unlike conventional delivery systems such as lipid nanoparticles or viral vectors [36]. This approach enables efficient therapeutic plasmid distribution, particularly within hypoxic tumor regions [37], while maintaining plasmid stability and functionality within host cells. The attenuated *Salmonella* strain employed was engineered for enhanced cytosolic plasmid release via *sifA* deletion and further attenuated by *lon* and *cpxR* deletions [38, 39]. Consistent with previous reports, this strain mediated plasmid delivery with approximately 100-fold greater efficiency than the wild-type strain, without inducing significant disease *in vivo*.

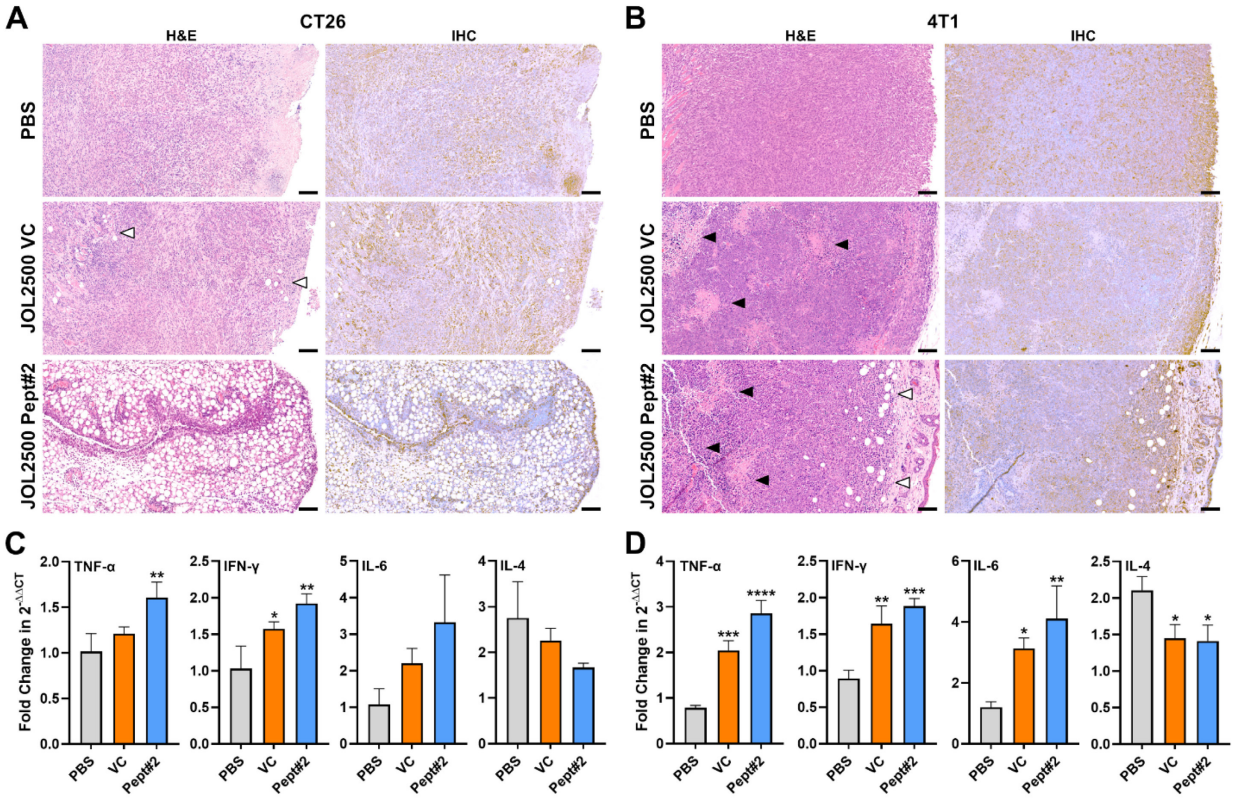

Figure 8. Histopathological evaluation of tumor disruption and LDHA expression following *Salmonella*-mediated therapy. (A, B) H&E and immuno-stained tumor sections from CT26 and 4T1 tumor-bearing mice. PBS group displayed densely packed cells with intact architecture. In contrast, JOL2500 Pept#2-treated tumors exhibit extensive necrosis, cellular shrinkage, and vacuolization. Corresponding IHC analysis of LDHA expression in CT26 and 4T1 tumors. Strong, diffuse DAB staining indicates high LDHA expression in control group, whereas Pept#2-treated tumors show a marked reduction in LDHA-positive staining. Images were acquired at equal magnification (scale bar = 100 μm). (C, D) RT-qPCR analysis of intratumoral cytokine expression (TNF-α, IFN-γ, IL-6, IL-4). Black arrowheads indicate necrotic/disrupted zones. White arrowheads indicate vacuolized zones. Asterisks denote significant differences compared to the PBS-treated group (*$p < 0.05$, **$p < 0.01$, ***$p < 0.001$, ****$p < 0.0001$).

Preliminary functional validation was performed using purified plasmids in *in vitro* transfection assays to exclude the confounding effects of *Salmonella*-induced cytotoxicity. These experiments were conducted using murine tumor cell lines, including CT26 colon carcinoma, B16F10 melanoma, and 4T1 mammary carcinoma. All four peptide constructs significantly suppressed cancer cell viability, with Pept#2 exhibiting the strongest activity (Fig. 1B and Fig. S1A-S1B). The physicochemical characteristics of Pept#2, particularly its reduced solubility and near-neutral net charge at pH 7, are consistent with its enhanced protein aggregation propensity (Table S4). As expected, Pept#2 demonstrated target specificity toward murine cancer cell lines while exerting no significant effects on human cancer cell lineage, reflecting phenotypic selectivity of Pept#2 (Fig. 1C-1E and Fig. 2A). Although mouse and human LDHA share substantial sequence homology, this selectivity indicates APR-induced aggregation may be sensitive to single-residue variations at the nucleation interface (Table S5).

LDHA is a critical driver of cancer metastasis and facilitates tumor cell invasion, migration, angiogenesis, and microenvironmental acidification [40]. Accordingly, LDHA suppression is anticipated to impair the metastatic potential. Consistent with this hypothesis, Pept#2 transfection significantly inhibited wound closure in CT26 cells, resulting in persistent cell-free gaps (Fig. 1D-1E), whereas no comparable effect was observed in non-target HeLa and Hep2 cells. Considering that normal cells rely minimally on aerobic glycolysis, off-target metabolic toxicity is expected to be limited. The functional integrity of Pept#2 was further confirmed using purified peptide formulations. Cytotoxic responses were pronounced in murine cancer cell lines (4T1 and CT26) but remained minimal in one human cancer cell lineage (HeLa), consistent with species-specific LDHA sequence differences (Fig. 2A). To determine how enhanced cytosolic accumulation affects cytotoxicity, chitosan nanoparticles were implemented as an in vitro delivery platform. The encapsulated peptide effectively induced apoptotic responses in 4T1 cells, although chitosan alone also contributed to apoptosis under stress conditions (Fig. 2B-2D).

Functional suppression of LDHA by Pept#2 was evidenced by an impaired compensatory glycolytic response following oligomycin and 2-DG challenge, resulting in reduced lactate production and profound

ATP depletion in treated cancer cells. In addition, direct enzymatic assays demonstrated a dose- and time-dependent inhibition of LDHA catalytic activity by Pept#2, supporting its role in disrupting aerobic glycolysis and metabolic flexibility in tumor cells (Fig. 3A-C). Furthermore, delivery of Pept#2 through the *Salmonella* vector enhanced apoptosis and oxidative stress in 4T1 cells, suggesting that combined bacterial delivery and LDHA inhibition intensify ATP starvation and mitochondrial dysfunction associated with impaired pyruvate metabolism (Fig. 4A-B).

The formation of protein aggregates following the LDHA - Pept#2 interaction was directly visualized by transmission electron microscopy (TEM). Due to its reduced solubility, Pept#2 readily promoted aggregate nucleation, appearing as a dense spherical structure in the TEM images (Fig. 5A). A stoichiometry-dependent activity of Pept#2 toward LDHA was observed, with maximal inhibition of cell acidification at 2 μg, whereas higher concentrations (20 μg) resulted in reduced inhibitory efficacy, likely due to peptide self-aggregation or intermolecular repulsion (Fig. 5B). These observations were further supported by the time- and concentration-dependent absorbance scans, which indicated enhanced aggregation at lower peptide concentrations (Fig. 5C). A progressive reduction in the soluble LDHA fraction was consistently observed over time (Fig. 5D).

Building on the *in vitro* findings, Pept#2 was evaluated in CT26 colon carcinoma and highly metastatic 4T1 mammary carcinoma models using the attenuated *Salmonella* JOL2500 delivery platform. Deletion of *lon* and *cpxR* enabled efficient tumor targeting, cellular invasion, and vacuolar escape while limiting chronic infection and maintaining host safety [38]. Tumor-bearing mice receiving booster doses of JOL2500 carrying the Pept#2 expression vector showed significant reductions in primary tumor growth and tumor mass compared with PBS and vector controls, without overt toxicity (Fig. 6A-6C and Fig. S4). In the 4T1 model, Pept#2 treatment also reduced metastatic burden in visceral organs and intestinal tissues, as evidenced by decreased splenic metastasis and tumor establishment in short-term analyses (Fig. 6D and Fig. 7C-7D). Although Fluo-4 AM is primarily a calcium-sensitive probe rather than a long-term cell tracker, our preliminary validation confirmed stable fluorescence in CT26 cells for up to 24 hours. Therefore, we utilized this dye to monitor the relative trends of metastatic cellular lodging within the pulmonary microvasculature following therapeutic administration. Unlike free peptide administration, which is often limited by rapid clearance and poor tumor penetration, *Salmonella*-mediated delivery enables sustained localized intracellular peptide expression within hypoxic tumor regions, thereby prolonging metabolic stress induced by LDHA aggregation.

During tumor excision, collapsed cores and cavitation were consistently observed in the Pept#2-treated groups, resulting the discrepancy between tumor mass and volume data (Fig. 6A-6C). Histopathological analysis of H&E-stained sections revealed dense, intact tumor architecture in the controls, whereas Pept#2-treated tumors exhibited extensive acellular spaces (white arrowheads) and necrotic regions (black arrowheads) (Fig. 8B). Marked pathological features, including widespread necrosis, stromal disintegration, vacuolization, nuclear pyknosis, karyorrhexis, and karyolysis, were prominent in treated tumors, but largely absent in controls. In CT26 tumors, Pept#2 treatment caused a loss of cellular cohesion and increased necrotic and stromal spaces, whereas 4T1 tumors displayed pronounced vacuolization, cytoplasmic shrinkage, and disruption of tissue architecture (Fig. 8A). These histological changes were consistent with LDHA aggregation-induced metabolic stress, leading to impaired lactate export, mitochondrial dysfunction, and oxidative imbalance, culminating in extensive tumor cell death and structural collapse [4].

Pept#2 treatment enhanced inflammatory signaling within tumors, characterized by increased TNF-α, IFN-γ, and IL-6 with minimal induction of IL-4, consistent with LDHA suppression, a central regulator of cancer metabolism (Fig. 8C-8D). Although tumor-associated inflammation can have dual roles, these findings suggest immunometabolic reprogramming following LDHA aggregation. By reducing lactate synthesis, Pept#2 may alleviate tumor acidosis, restore cytotoxic immune cell function, and enhance immune cell infiltration, thereby extending its effects beyond direct tumor cytotoxicity. The lactate production and glycolysis/OXPHOS ATP production assay provided a direct functional readout of LDHA inhibition, validating peptide-mediated enzymatic disruption through dose-dependent lactate suppression (Fig. 3). These results highlight the promise of reverse-engineered aggregation-prone peptides as a versatile therapeutic strategy, offering high specificity through targeted disruption of protein assembly, applicability to traditionally undruggable targets, and adaptability via rational peptide design and advanced delivery platforms. Although Pept#2 was designed from murine LDHA motifs and demonstrated species-selective activity, the core APR motif is highly conserved in human LDHA (12/13 AA; 92.3%) (Fig. S7). Despite the homology, Pept#2 induced apoptosis and metabolic alteration in murine cancer cell lines while having negligible effects on

human cancer cells. In peptide-induced protein aggregation, β-strand intercalation and steric zipper formation are notoriously sensitive to single-residue alterations, which can impose a sequence barrier that restricts cross-species aggregation [41, 42]. The key catalytic and oligomerization interfaces of LDHA are functionally and structurally preserved across species, supporting the broader adaptability of this aggregation-based strategy. Acknowledging that the current murine-specific sequence limits immediate clinical application, our future work will focus on identifying human-specific APR motifs using computational aggregation prediction and structural modeling. The modular nature of *Salmonella*-based delivery platforms enables a straightforward peptide substitution without altering the vector framework, thereby facilitating rapid translational adaptation.

Although apoptosis levels may appear modest in isolation, they reflect a broader metabolic stress response induced by LDHA inactivation, which disrupts the redox balance, elevates reactive oxygen species, and restricts biosynthetic precursors. This metabolic vulnerability sensitizes tumor cells to immune-mediated clearance and conventional therapies, positioning Pept#2 as a metabolic disruptor rather than a cytotoxic agent. Accordingly, combination strategies with immunotherapy, chemotherapy, or radiotherapy may further enhance efficacy. Given the heterogeneity of LDHA expression across tumors, patient stratification using LDHA levels or lactate signatures may improve clinical responsiveness. The integration of metabolic biomarkers, imaging, and transcriptomic profiling is essential for clinical translation, whereas the modular *Salmonella* delivery platform enables multi-target metabolic interventions to address tumor heterogeneity. Despite its strengths, this study has several limitations. The lack of real-time metabolic flux analyses and *in vivo* lactate measurements warrants further investigation. Accurate *in vivo* lactate and ATP production is precluded by post-mortem ischemic artifacts that induce artificial glycolytic surges, as well as the metabolic heterogeneity inherent in solid tumors which bulk-tissue analysis cannot resolve. Given these technical limitations, we prioritized *in situ* IHC analysis, which provides direct visual confirmation of peptide-mediated LDHA structural degradation within the tumor tissue. We acknowledge the need for future specialized stable-isotope tracing to achieve high-resolution metabolic flux profiling *in vivo*. Because metabolic plasticity may enable compensatory utilization of oxidative phosphorylation or alternative lactate dehydrogenase isoforms, future studies should evaluate adaptive metabolic rewiring following prolonged LDHA aggregation. Although functional data support aggregation-mediated LDHA inactivation, direct *in vivo* visualization of LDHA aggregates would strengthen our mechanistic insights. Future studies should also focus on validating LDHA aggregation *in vivo*, characterizing immune modulation within the TME, redesigning APR peptides for human LDHA specificity, and evaluating combination therapies to advance clinical translation.

Conclusion

In summary, this study demonstrates that *Salmonella*-delivered APR peptides can effectively suppress LDHA activity through aggregation-mediated functional inactivation, leading to a significant reduction in lactate synthesis. This strategy represents a novel and mechanistically distinct approach for targeting cancer metabolism and overcoming the many limitations of conventional LDHA inhibitors. By integrating metabolic disruption with bacterial delivery, this platform offers a promising avenue for durable tumor control and future translational development.

Materials and methods

Bacterial strains, plasmids, and primers

All bacterial strains, plasmids, and primers used in this study are listed in Table. S1. The *Salmonella* delivery strain, JOL2500 (*Salmonella* Typhimurium Δ*lon*, Δ*cpxR*, Δ*sifA*, Δ*asd*), and eukaryotic expression plasmid, pJHL204, used in this study were characterized in previous study [43]. Briefly, the JOL2500 strain acts as a tumor-tropic carrier, enabling intracellular plasmid delivery through bacterial invasion [44]. Once the plasmid released within cells, the RdRp circuit induces robust cytoplasmic mRNA amplification and enhanced expression of encoded peptide. *Escherichia coli* and *Salmonella* Typhimurium strains were routinely grown in Luria-Bertani (LB; BD, Franklin Lakes, NJ, USA) medium, broth, or as LB agar at 37 ℃, with or without vigorous shaking. Antibiotic ampicillin was added at 100 μg/mL for selection purposes. Bacterial strains were stored as glycerol stocks (15–20% glycerol) at –80 °C and revived on LB agar before use.

Cell culture models

Mouse and human cancer cell lines were used to establish *in vitro* cell culture models and evaluate their efficacy and specificity. The murine colon carcinoma cell line CT26 (ATCC; CRL-2638), melanoma cell line B16F10 (ATCC; CRL-6475) and breast cancer cell line 4T1 (ATCC; CRL-2539) were used as target cell models, whereas human-derived cell lines, including

HeLa (cervical carcinoma, ATCC; CCL-2), and Hep2 (laryngeal carcinoma, ATCC; CCL-23), served as non-target controls. All cell lines were cultured in Dulbecco's modified Eagle's medium (DMEM; Gibco, USA) supplemented with 10% fetal bovine serum (FBS; Gibco) and 1% penicillin-streptomycin. Cells were maintained at 37 °C in a humidified incubator with 5% CO_2 and subcultured every 2–3 d to ensure exponential growth and optimal viability for downstream experiments.

Experimental animals and ethics statement

Five-week-old SPF female mice were purchased from Samtako (Osan-Si, Gyeonggi-do, South Korea) and housed in an animal facility with a 12 h day and night cycle. The mice were provided food and water ad libitum. This study was approved by the Jeonbuk National University Animal Ethics Committee (NON2022-024-002) under the Korean Council on Animal Care and the Korean Animal Protection Law 2001, Article 13.

Peptide design and prediction of APR

Prediction of APRs within LDHA isoforms 1 and 2 was done in silico using the Tango algorithms, a validated computational tool for predicting β-sheet-mediated aggregation tendencies in amino acid sequences [16, 45]. Full-length amino acid sequences of LDHA isoforms were retrieved from the UniProt database and input into TANGO with the default parameters optimized for physiological conditions (pH 7.4, 298 K, ionic strength 0.02 M). The predicted APRs were assessed based on aggregation score thresholds, and candidate regions common to both LDHA isoforms 1 and 2 were shortlisted. Peptides were designed based on these conserved APRs with careful evaluation of their physicochemical properties, including hydrophobicity, charge distribution, and structural compatibility. Further screening was performed to ensure sequence specificity, avoid off-target effects, and reduce immunogenicity by selecting the lowest possible number of residues. Four peptides demonstrating high aggregation potential, specificity for LDHA isoforms, and favorable homology across isoforms were selected for further analysis. These candidates were prioritized based on a combination of prediction accuracy, isoform coverage, and minimal sequence redundancy. The selected sequences are listed in the Table. S2.

Peptide synthesis, cloning, and construct verification

Four selected peptide sequences targeting APRs of LDHA isoforms 1 and 2 were commercially synthesized by CosmoGene (Seoul, South Korea). Each peptide-encoding DNA fragment was codon-optimized for mammalian expression and synthesized with the appropriate restriction enzyme (RE) sites flanking the sequences to facilitate cloning. The synthesized fragments were cloned into the mammalian expression vector pcDNA3.2 using BamHI and EcoRI restriction enzyme sites. Recombinant plasmids were ligated using T4 DNA ligase and transformed into *Escherichia coli* DH5α competent cells via the heat-shock method. Transformants were selected on Luria-Bertani (LB) agar plates supplemented with ampicillin (100 μg/mL), and positive colonies were screened for the presence of inserts. Colony PCR was performed using vector-specific primers to confirm the presence of inserted peptide sequences. Additionally, plasmid DNA was extracted from positive clones using a miniprep kit (GeneAll, Daejeon, South Korea), followed by restriction enzyme digestion with BamHI and EcoRI to confirm the correct insert orientation and size. The digested products were analyzed by agarose gel electrophoresis.

Cytotoxicity assay

The anticancer efficacy of the designed peptides was evaluated based on their cytotoxicity upon transfection. Murine cancer cell lines CT26, B16F10, and 4T1 were propagated and seeded in 96-well plates at 1×10^4 cells/well and incubated for 24 h. Following the manufacturer's protocol, plasmids cloned with Pept#1, 2, 3, and 4 were transfected into cell monolayers at a 1 μg/ well concentration using LyoVec (InvivoGen, San Diego, CA, USA). After 24 h of incubation, the number of viable cells was quantified using the EZ-Cytox cell viability assay (DogGenBio, Geumcheon-gu, Seoul, South Korea). The endpoint absorbance was measured at 450 nm. The experiment was conducted in triplicate, and the average was compared to PBS treatment groups.

Live-cell cytotoxicity assay using PI staining

The specificity of the peptide effect on murine cell lines was evaluated by PI staining of late apoptotic cells [46], which was conducted as a real-time imaging study using the IncuCyte live imaging system (Essen Bioscience, Gottingen, Germany). The CT26 murine cancer cell line was compared with human carcinoma Hep2 and HeLa cells grown in 12-well plates. After 24 h incubation, cells were transfected with pcDNA3.2::Pept#2, the best responder at 1.5 μg/ well, using the LyoVec procedure and further incubated for 12 h. Cell medium was replaced and replenished with complete medium containing PI (5 μg/ mL) and observed in real-time using the IncuCyte. Changes in apoptotic cells (red spots) were evaluated and

compared with the VC and medium only (MO) group. All experiments were conducted in triplicate, and the results were presented as mean ± standard deviation.

Synthesis of pure peptide and assessment of cell internalization

The FLAG-tag-truncated version of the most effective APR peptide, Pept#2 (33 AA), was synthesized for downstream characterization (Cusabio Technology LLC, Houston, TX, USA). The identity and purity of peptide were validated by the manufacturer using mass spectrometry (MS) and high-performance liquid chromatography (HPLC), confirming >95% purity. The solubility of the peptide sequence was low; hence, solubilization was performed by initiation with ultrapure water with vigorous agitation while slowly adding up to 6% (v/v) dimethyl sulfoxide. Intermittent heating at 42 ℃ was used to facilitate solubilization.

To clarify the cell internalizing property of Pept#2, the immunofluorescence analysis was performed. Briefly, the CT26 cells were plated and attached on slide glass, then treated with purified Pept#2 peptides in 0, 1 and 5 µg/mL dosage for 15 min. The treated cells were fixed with 4% paraformaldehyde solution for 10 min and then permeabilized with 0.1% (v/v) Triton X-100 in PBS solution for 10 min. After washing, the blocking buffer, 1% BSA in PBS, was added to the cells and incubated for 1 hr. The anti-FLAG tag monoclonal mouse antibody (Invitrogen, Carlsbad, CA, USA) was utilized as primary antibody in 1:200 dilution. The secondary antibody solution was added onto the cells in 1:1,000 dilutions. The goat anti-mouse IgG conjugated with Alexa Fluor™ 647 (Thermofisher scientific, Massachusetts, USA) was utilized as secondary antibody. Nuclei were counterstained with DAPI in 0.5 µg/mL for 5 min. The prepared slides were analyzed using confocal laser scanning microscope, LSM 880 with Airyscan (Carl Zeiss, GmbH, Germany) (Fig. S2).

Characterization of pure peptide

The cytotoxicity induced by the pure form of Pept#2 was evaluated in murine cancer cells (4T1 and CT26 cells as target cell lines) and human cancer cell lines (Hep2 and HeLa as non-target cell lines). To determine the therapeutic window and evaluate dose-dependent efficacy, the peptide was tested across a concentration gradient ranging from 0.025 to 5 µg/mL. The gradient concentrations were selected based on preliminary solubility and dose-screening assessment. Each cell line was seeded in a 96-well plate at a density of 10^4 cells/well. Cells were incubated overnight and treated with varying concentrations of the peptide. Treated cells were further incubated for 24 h and cytotoxic responses were evaluated using a standard cytotoxicity assessment procedure with the EZ Cytox assay. The data were plotted, and the effects of peptide treatment on target and non-target cells were evaluated.

To assess the impact of enhanced cellular permeability and cytosolic internalization on the efficacy of peptide, the chitosan ionic gelation was performed as described in a previous study [47]. The effects of the encapsulated peptide were evaluated using the Annexin V/PI (BD Pharmingen FITC Annexin V Apoptosis Detection, Franklin Lakes, NJ, USA) apoptosis assay and H_2-DCFDA (Thermo, Waltham, MA, USA) assay, following the procedures described elsewhere [48, 49]. The induction of apoptosis and oxidative stress was visually observed using fluorescence microscopy and quantified using flow cytometry (Macsquant, Bergisch Gladbach, Germany).

Biochemical confirmation of LDHA functional suppression by absorbance

LDHA enzymatic activity was evaluated by monitoring the oxidation of NADH to NAD^+, which was measured and represented by a decrease in absorbance at 340 nm. Recombinant LDHA was used at a constant concentration of 5 µg per reaction under all experimental conditions. The anticancer peptide (Pept#2) was added at varying concentrations, 1, 2, 3, 4, and 5 µg per reaction, to investigate the dose-dependent suppression of LDHA activity. Experimental controls–no LDHA, LDHA alone, or LDHA co-incubated with peptides–were used. The LDHA and peptide were incubated together in equal volumes (5 µL each) to make a total of 10 µL per reaction. The reaction mixture was then incubated for 20 min at room temperature. Following incubation, the enzymatic reaction was initiated by adding a reaction mixture containing NADH (final concentration 0.1 mM; stock 10 mM; Sigma) and sodium pyruvate (final concentration 1 mM; stock 100 mM; Sigma) to comprise 400 µL total volume. As soon as the reaction was initiated, each reaction volume was aliquoted into UV-transparent 96-well plates using 100 µL per well and immediately measured for the absorbance at 340 nm wavelength. The pattern of NADH absorbance correlated with the plausible inhibition of LDHA. The inhibitory potency of Pept#2 against LDHA was quantified by determining the IC_{50} value. The initial reaction velocity (V_0) for LDHA was calculated from the linear slope of NADH consumption (absorbance decrease at 340 nm) over the first 120 seconds. Relative enzyme activity (%) was normalized to the vehicle control (0 µg peptide). These values were plotted

against the logarithmic concentration of the peptide. The IC_{50} was calculated using non-linear regression analysis with a variable slope (four-parameter logistic curve) using GraphPad Prism 8.0 via the following equation.

Biochemical confirmation of suppression effect on cellular ATP production and lactate synthesis

The APR peptide-mediated effects on ATP production were analyzed using a glycolysis/OXPHOS assay kit (Dojindo Laboratories, Kumamoto, Japan). The assay was performed according to the manufacturer's instructions. Briefly, murine cancer (4T1 and CT26) and human cancer (HeLa and Hep2) cells were plated in 96-well white microplates at 3×10^3 cells/well density. The cells were treated with only media and media containing 5 µg/mL of Pept#2 for 24 h. The Pept#2 treated and non-treated wells were then divided into three groups and treated with media supplemented with oligomycin or 2-DG (2-Deoxy-D-glucose) for 5 h, indicating oligomycin (–) 2-DG (–), oligomycin (+) 2-DG (–), and oligomycin (–) 2-DG (+). After incubation, 20 µl media was collected and used for lactate production assay. The working solution was added to the remaining cell media and shaken for 2 min. The assay plate was incubated for 10 min at room temperature, and luminescence was measured. Data were normalized to the levels in cells cultured without oligomycin or 2-DG.

Safety assessment of pure Pept#2

The safety of the therapeutic peptide was predicted using in silico methods and a hemolysis assay using defibrinated sheep blood (MB Cell, Seoul, South Korea). Two percent sheep blood was prepared in sterile PBS and used as red blood cells (RBCs) in PBS (negative control), RBCs in 0.1% Triton X-100 (positive control), and increasing concentrations of APR Pept#2 (from 1 to 5 µg co-mixed with RBCs). All reaction conditions were made in a 400 µL volume and incubated for 1 h at 37 ℃. After incubation, images were taken before and after centrifugation at 1500 RPM for 5 min, and the absorbance of the supernatant was measured at 540 nm. The percentage of hemolysis was measured using the following formula: hemolysis (%) = $(Abs_{sample} - Abs_{PBS})/(Abs_{Tx100} - Abs_{PBS}) \times 100$. Furthermore, in silico tools such as ProtParam [50], PeptideRanker [51], ToxinPred [52], and HemoPI [53] have been used to assess biological compatibility.

Docking and molecular interaction analysis

To confirm that APR Pept#2 interacted with LDHA isoforms 1 and 2, a molecular docking study was conducted. Mouse LDHA isoforms 1 and 2 sequences were retrieved from the National Center for Biotechnology Information (NCBI) database [54] and modelled by submitting them to the SWISS Model server [55]. The model for Pept#2 was derived from the Phyre2 server after running in intensive mode. Protein and peptide docking analyses were conducted using the Zdock server [56], without specifying interacting residues. Visualization of the predicted interactions was performed using the Discovery Studio Client [57].

To investigate the structural basis of peptide-LDHA interactions and species selectivity, molecular docking of Pept#2 with mouse and human LDHA was performed using HDOCK pipeline [58, 59]. The 3D structure models of mouse and human LDHA wee subjected to pipeline. Targeted molecular docking was performed by specifying the target aggregation-prone region (APR) sequence as the designated binding constraint on both LDHA orthologs. Docking simulations were computed using the hybrid docking algorithm implemented in HDOCK, combining template-based modeling with *ab initio* free docking. The resulting docking conformations were ranked based on the HDOCK scoring function (energy scores and shape-complementarity metrics), and the top-ranked conformation (Model 1) was selected for detailed interaction profiling. Receptor–ligand interface residues, contact networks, and interatomic distances (Å) were analyzed.

APR peptide effect alongside *Salmonella*

The engineered strains were used to evaluate the effect of Pept#2 on cancer cells via *Salmonella* delivery. *Salmonella* infection was performed on 4T1 monolayers grown in 24-well plates at a multiplicity of infection (MOI) of 40%. After two hours of incubation, cell monolayers were washed with PBS and treated with gentamycin (150 µg/mL) to eliminate non-invaded bacteria. After two hours of incubation, cells were washed and supplemented with fresh complete media containing 50 µg/mL gentamycin and incubated for 8 h. Cell apoptosis was assessed by flow cytometry.

Wound healing assay for assessment of anti-metastatic activity and cell specificity

To evaluate the impact of peptide expression on cancer cell migration and specificity, wound healing assays were performed using CT26 murine colon carcinoma cells as target cells and HeLa and Hep2 cells as non-target controls. Cells were cultured in their respective recommended growth media supplemented with 10% fetal bovine serum and 1% penicillin-streptomycin, and maintained under standard incubator conditions (37 °C, 5% CO_2). Cells

were seeded into 6-well plates and allowed to reach near-confluent monolayers. A uniform scratch was made across the center of each well using a sterile 200 µL pipette tip to simulate a wound. Detached cells were removed by washing with PBS, and cells were then transfected with the respective peptide-expressing plasmids using Lyovec™ transfection reagent, following the manufacturer's instructions. The control group included cells treated with Lyovec alone and those transfected with the empty pcDNA3.2 vector. After transfection, a serum-free medium was added to minimize proliferation-induced wound closure. Images of the wound area were captured at 0, 24, and 48 h, using a phase-contrast microscope. Wound closure was quantified using the ImageJ software by measuring the gap width at each time point and calculating the percentage of wound closure relative to the initial wound size. The anti-migratory effect was considered significant if wound closure was inhibited in CT26 cells, while minimal or no effect in HeLa and Hep2 cells indicated the target-specific action of the peptide constructs.

Preparation of the LDHA protein

The open reading frame of mouse LDHA (AAH94019.1) was amplified using cDNA generated from the total RNA of CT26 mouse colon cancer cells. The primers used for amplification are listed in Table S1. The PCR product was cloned into the pET28a+ plasmid system (Novagen; Merck Millipore, Burlington, MA, USA) using the BamH1 and EcoR1 restriction sites for protein expression. The resulting plasmid was screened and transformed into Escherichia coli BL21(DE3) cells for protein induction. Protein expression was induced with 2 mM Isopropyl β-D-1-thiogalactopyranoside (IPTG; St. Louis, MO, USA) at 30 °C for six hours. Purification was performed using Ni-NTA resin (Qiagen, Hilden, USA) under denaturing conditions with 8 M urea. Protein refolding was achieved by overnight dialysis against excess PBS at 4 °C. Protein concentrations were measured using the Bradford assay [60]. Aliquots of proteins were stored at -20 ℃ for further use.

Electron microscopy evaluation of peptide-induced aggregates

To evaluate the ultramicroscopic phenotype of the protein aggregates, we performed electron microscopy of the aggregated proteins. Dialyzed LDHA protein samples were filtered through 0.2 µm membrane filters (Biofact, Yuseong-gu, Daejeon, South Korea). Twenty-five micrograms of protein were co-incubated with 4 µg of solubilized pure peptide (Pept#2). The solution was mixed by pipetting firmly and incubated overnight at 4 °C. Ten microliters of the co-incubated solution were placed on a carbon-coated copper grid and incubated for 5 min. Grids were washed with ultrapure water three times by placing 10 µL of water on the grid each time. Excess solution was removed using filter paper absorbent pads. After adsorption, negative staining was performed with 10 µL of uranyl acetate (Sigma, St. Louis, MO, USA) for 5 seconds. Excess solution was removed by absorption onto filter paper. The samples were visualized using a Bio-TEM (Hitachi, Tokyo, Japan) at an acceleration voltage of 100 kV and 100,000× magnification.

Assessment of the impact on cell acidification

The effect of peptide treatment on cancer cell acidification trends was evaluated using a BCECF-AM assay (Thermo Scientific, Waltham, MA, USA) on CT26 cells. CT26 colon cancer cells were seeded in 24-well plates at a density of 2×10^4 cells/well and incubated. When the cell confluence exceeded 70%, cells were treated with pure peptide (Pept#2) at concentrations of 0, 5, 10, and 20 µg per well and incubated for six hours. Cells were washed with DMEM alone, then replaced with DMEM containing 2% FBS, and stained directly with BCECF-AM at a 2 µM concentration. Cells were then incubated for 20 min at 37 °C in a 5% CO_2 atmosphere. The plates were protected from light and washed twice with medium. Cells were observed under a fluorescence microscope (red fluorescence), and images were captured for comparison (excitation 440 nm, EM 535 nm). Fluorescence intensity was quantified using ImageJ Fiji software 41.

Assessment of protein aggregation kinetics

To conduct an absorbance scan during protein aggregation, an absorbance scan was conducted between 280 and 460 nm in 10 nm increments each time using a plate reader (Tecan, Mannedorf, Switzerland). A suspension was created by taking 80 µL of filtered ultrapure water, 20 µg of purified LDHA, and incremental levels of pure peptide solution (Pept#2) at 2, 4, and 10 µg per reaction. The total reaction volume was balanced to 110 µL and allowed to co-incubate for 2, 5, 10, and 120 min in order to capture early and late aggregation kinetics. Absorption measurements were normalized to water and the LDHA control. Absorbance measurements were evaluated with respect to the peptide concentration and time. Furthermore, variations in the soluble fraction of the protein were investigated by measuring the absorbance at 280 nm.

In vivo analysis of cancer reduction using metastatic tumors

To evaluate the effect of the engineered therapeutic strains on implanted cancer growth, 4T1 and CT26 cell lines were evaluated in a BALB/c mouse model (N = 32, n = 4). The study cohorts included three experimental groups (PBS, JOL2500 VC, and JOL2500 Pept#2) and a naïve group for baseline comparison in each cell line study. The mice were inoculated with exponentially growing 4T1 cells at a dose of 10^6 cells/mouse in 100 µL PBS, which was placed under the skin of the ventral lower left quadrant of the body. After 10 days of growth, the mice were intraperitoneal (IP)-treated with JOL2500 Pept#2, JOL2500 VC or PBS. Mice were boosted two weeks after primary inoculation. At 12-days post booster, all mice were euthanized, and tumor tissues were harvested for histopathological examination and measurements. The spleens were harvested separately to compare the effects of *Salmonella* treatment.

For metastatic cancer inhibition assay in longitudinal period, we used the 4T1 breast cancer cell line as metastatic cancer cell line. The female BALB/c mice (N = 9, n = 3) were acclimatized for one week and inoculated with the therapeutic *Salmonella* strain via IP route, 1×10^6 CFU/mouse prepared in 100 µL PBS. After three days, 4T1 cancer cells were tail vein inoculated into immunized mice at 1×10^6 cells/mouse in 100 µL PBS. Mice were boosted with therapeutic *Salmonella* two weeks after primary inoculation. After another week, all mice were euthanized, and the visceral organs were investigated for tumoral nodule screening by histopathological and macroscopic analysis.

The effect of JOL2500 Pept#2 on metastasis inhibition was evaluated by short-term metastasis assay. Three days after the IP inoculation of therapeutic *Salmonella*, CT26 cancer cells stained with Fluo-4AM cell-tracking dye (Thermo Scientific) were introduced via the tail vein. After 12 h, the mice were euthanized and subjected to flow cytometry analysis of the lung cell population.

Histopathological analysis

Histopathological analysis was performed on tissue samples collected from the experimental mice at the study endpoint using an eosin and hematoxylin staining procedure as described elsewhere with some modifications [61, 62]. Briefly, the excised tissues were immediately fixed in 10% neutral-buffered formalin for 24-48 h at room temperature. After fixation, samples were dehydrated using a graded ethanol series, cleared in xylene, and embedded in paraffin wax. Sections of 5 µm thickness were cut using a microtome and mounted on glass slides. Tissue sections were deparaffinized, rehydrated, and stained with hematoxylin for nuclear visualization, followed by eosin staining for cytoplasmic contrast. The stained slides were examined under a light microscope to assess tissue morphology, inflammation, necrosis, and other pathological features associated with tumor development or systemic immune responses.

Immunohistochemistry to quantify intact LDHA in tumor tissue

IHC was performed to visualize APR-mediated LDHA degradation. Tumor tissues mounted on glass slides were immunostained as previously described [63]. Briefly, sections were incubated with polyclonal anti-LDHA rabbit antibody (1:30 dilution), followed by a goat anti-rabbit IgG secondary antibody conjugated with horseradish peroxidase (HRP) (1:3,000 dilution). The 3,3′-diaminobenzidine (DAB) substrate was used for LDHA development. To quantify intact LDHA, DAB-stained pixels were processed for threshold adjustment to 40 % and measured using ImageJ software.

Real-time PCR for inflammatory markers

A portion of the tumor tissue was used for total RNA isolation. Tissue sections were aseptically recovered, washed with cell culture medium, and homogenized in RiboX solution. RNA was isolated using a commercial kit (GeneAll Hybrid-R, Daejeon, South Korea) following the manufacturer's protocol. RNA quantification was done, and 1 µg of RNA was converted into cDNA (Elpis Bio, Daejeon, South Korea). Synthesis of cDNA was used in real-time polymerase chain reaction (RT-qPCR) analysis to evaluate a few selected cytokine markers, TNF-α, IFN-γ, IL-4, and IL-6 (Table S1).

Statistical analysis

Data analysis was performed using the Python statistical package. Significant differences between the treated and control groups were assessed using a one-way analysis of variance (ANOVA) followed by Dunnett's multiple comparisons test. Statistical significance was set at $p < 0.05$. * $p < 0.05$, ** $p < 0.01$, *** $p < 0.001$, and **** $p < 0.0001$.

Supplementary Material

Supplementary figures and tables.
https://www.ijbs.com/v23p0507s1.pdf

Acknowledgements

This research was supported by the National Research Foundation of Korea (NRF) grant funded by the Korean government (MSIT) (No RS-2023-00272216).

Data availability

All raw data can be made available upon request.

Author contributions

K.J., performing experiments, analysis, and writing the manuscript. A.S., research design, performing experiments, analysis, and writing the manuscript. M.B., performing experiments and writing the manuscript. J.H.L., supervision, fund acquisition.

Competing Interests

The authors have declared that no competing interest exists.

References

1. Wu Z, Xia F, Lin R. Global burden of cancer and associated risk factors in 204 countries and territories, 1980-2021: a systematic analysis for the GBD 2021. J Hematol Oncol. 2024; 17: 119.
2. Zhang W, Wang C, Hu X, Lian Y, Ding C, Ming L. Inhibition of LDHA suppresses cell proliferation and increases mitochondrial apoptosis via the JNK signaling pathway in cervical cancer cells. Oncol Rep. 2022; 47.
3. Liberti MV, Locasale JW. The Warburg Effect: How Does it Benefit Cancer Cells? Trends Biochem Sci. 2016; 41: 211-8.
4. Le A, Cooper CR, Gouw AM, Dinavahi R, Maitra A, Deck LM, et al. Inhibition of lactate dehydrogenase A induces oxidative stress and inhibits tumor progression. Proc Natl Acad Sci U S A. 2010; 107: 2037-42.
5. Jafary F, Ganjalikhany MR, Moradi A, Hemati M, Jafari S. Novel Peptide Inhibitors for Lactate Dehydrogenase A (LDHA): A Survey to Inhibit LDHA Activity via Disruption of Protein-Protein Interaction. Sci Rep. 2019; 9: 4686.
6. Navas LE, Carnero A. NAD(+) metabolism, stemness, the immune response, and cancer. Signal Transduct Target Ther. 2021; 6: 2.
7. Luo M, Ma X, Ye J. Reductive stress-a common metabolic feature of obesity and cancer. Acta Pharm Sin B. 2024; 14: 5181-5.
8. Yang H, Yang S, He J, Li W, Zhang A, Li N, et al. Glucose transporter 3 (GLUT3) promotes lactylation modifications by regulating lactate dehydrogenase A (LDHA) in gastric cancer. Cancer Cell Int. 2023; 23: 303.
9. El Hassouni B, Franczak M, Capula M, Vonk CM, Gomez VM, Smolenski RT, et al. Lactate dehydrogenase A inhibition by small molecular entities: steps in the right direction. Oncoscience. 2020; 7: 76-80.
10. Pham CL, Kwan AH, Sunde M. Functional amyloid: widespread in Nature, diverse in purpose. Essays Biochem. 2014; 56: 207-19.
11. Bourgade K, Frost EH, Dupuis G, Witkowski JM, Laurent B, Calmettes C, et al. Interaction Mechanism Between the HSV-1 Glycoprotein B and the Antimicrobial Peptide Amyloid-beta. J Alzheimers Dis Rep. 2022; 6: 599-606.
12. Eimer WA, Vijaya Kumar DK, Navalpur Shanmugam NK, Rodriguez AS, Mitchell T, Washicosky KJ, et al. Alzheimer's Disease-Associated beta-Amyloid Is Rapidly Seeded by Herpesviridae to Protect against Brain Infection. Neuron. 2018; 100: 1527-32.
13. van der Kant R, Karow-Zwick AR, Van Durme J, Blech M, Gallardo R, Seeliger D, et al. Prediction and Reduction of the Aggregation of Monoclonal Antibodies. J Mol Biol. 2017; 429: 1244-61.
14. Jafary F, Moradi A, Ganjalikhany MR, Hassanpour Dehnavi A, Seifati SM, Khodarahmi A, et al. Investigation of the inhibitory peptide effect as novel strategy in cancer treatment: Targeting the tetramerization of lactate dehydrogenase A. Int J Biol Macromol. 2025; 306: 140878.
15. Nguyen VH, Min JJ. Salmonella-Mediated Cancer Therapy: Roles and Potential. Nucl Med Mol Imaging. 2017; 51: 118-26.
16. Lu X, Brickson CR, Murphy RM. TANGO-Inspired Design of Anti-Amyloid Cyclic Peptides. ACS Chem Neurosci. 2016; 7: 1264-74.
17. Wang X, Das TK, Singh SK, Kumar S. Potential aggregation prone regions in biotherapeutics: A survey of commercial monoclonal antibodies. MAbs. 2009; 1: 254-67.
18. Michiels E, Roose K, Gallardo R, Khodaparast L, Khodaparast L, van der Kant R, et al. Reverse engineering synthetic antiviral amyloids. Nat Commun. 2020; 11: 2832.
19. Dunham AS, Beltrao P. Exploring amino acid functions in a deep mutational landscape. Mol Syst Biol. 2021; 17: e10305.
20. Zhu Z, Pan F, Wang O, Zhao L, Zhao L. Antibacterial Effect of Sesame Protein-Derived Peptides against Escherichia coli and Staphylococcus aureus: In Silico and In Vitro Analysis. Nutrients. 2024; 16.
21. Zapadka KL, Becher FJ, Gomes Dos Santos AL, Jackson SE. Factors affecting the physical stability (aggregation) of peptide therapeutics. Interface Focus. 2017; 7: 20170030.
22. Yoshida T, Sakakibara N, Ura T, Minamiki T, Shiraki K. Cationic polyelectrolytes prevent the aggregation of l-lactate dehydrogenase under unstable conditions. Int J Biol Macromol. 2024; 257: 128549.
23. Aganja RP, Sivasankar C, Hewawaduge C, Lee JH. Safety assessment of compliant, highly invasive, lipid A-altered, O-antigen-defected Salmonella strains as prospective vaccine delivery systems. Vet Res. 2022; 53: 76.
24. Astm F. 756-00. Standard practice for assessment of hemolytic properties of materials. Philadelphia: American Society for Testing and Materials. 2000.
25. De Leon-Oliva D, Gonzalez-Prieto P, De Castro-Martinez P, Boaru DL, Laguna-Hernandez P, Fraile-Martinez O, et al. Revisiting the biological role of the Warburg effect: Evolving perspectives on cancer metabolism. Pathol Res Pract. 2025; 273: 156151.
26. Shibata S, Sogabe S, Miwa M, Fujimoto T, Takakura N, Naotsuka A, et al. Identification of the first highly selective inhibitor of human lactate dehydrogenase B. Sci Rep. 2021; 11: 21353.
27. Boudreau A, Purkey HE, Hitz A, Robarge K, Peterson D, Labadie S, et al. Metabolic plasticity underpins innate and acquired resistance to LDHA inhibition. Nature Chemical Biology. 2016; 12: 779-86.
28. Sharma D, Singh M, Rani R. Role of LDH in tumor glycolysis: Regulation of LDHA by small molecules for cancer therapeutics. Seminars in Cancer Biology. 2022; 87: 184-95.
29. Zheng Q, Xie Y, Xu L, Chen D, Wu J, Liu S, et al. LDHA as a predictive biomarker and its association with the infiltration of immune cells in pancreatic adenocarcinoma. J Gastrointest Oncol. 2024; 15: 1746-59.
30. Mishra D, Banerjee D. Lactate Dehydrogenases as Metabolic Links between Tumor and Stroma in the Tumor Microenvironment. Cancers (Basel). 2019; 11.
31. Tang Y, Gu S, Zhu L, Wu Y, Zhang W, Zhao C. LDHA: The Obstacle to T cell responses against tumor. Front Oncol. 2022; 12: 1036477.
32. Feng Y, Xiong Y, Qiao T, Li X, Jia L, Han Y. Lactate dehydrogenase A: A key player in carcinogenesis and potential target in cancer therapy. Cancer Med. 2018; 7: 6124-36.
33. Wang ZH, Peng WB, Zhang P, Yang XP, Zhou Q. Lactate in the tumour microenvironment: From immune modulation to therapy. EBioMedicine. 2021; 73: 103627.
34. Du M, Yu T, Zhan Q, Li H, Zou Y, Geng M, et al. Development of a novel lactate dehydrogenase A inhibitor with potent antitumor activity and immune activation. Cancer Sci. 2022; 113: 2974-85.
35. Wu H, Huang J. Optimization of protein and peptide drugs based on the mechanisms of kidney clearance. Protein and peptide letters. 2018; 25: 514-21.
36. Aganja RP, Sivasankar C, Senevirathne A, Lee JH. Salmonella as a Promising Curative Tool against Cancer. Pharmaceutics. 2022; 14.
37. Roland KL, Brenneman KE. Salmonella as a vaccine delivery vehicle. Expert Rev Vaccines. 2013; 12: 1033-45.
38. Kirthika P, Senevirathne A, Jawalagatti V, Park S, Lee JH. Deletion of the lon gene augments expression of Salmonella Pathogenicity Island (SPI)-1 and metal ion uptake genes leading to the accumulation of bactericidal hydroxyl radicals and host pro-inflammatory cytokine-mediated rapid intracellular clearance. Gut Microbes. 2020; 11: 1695-712.
39. Shetty D, Abrahante JE, Chekabab SM, Wu X, Korber DR, Vidovic S. Role of CpxR in Biofilm Development: Expression of Key Fimbrial, O-Antigen and Virulence Operons of Salmonella Enteritidis. Int J Mol Sci. 2019; 20.
40. Stepanov YV, Solyanik GI, Yakshibaeva Y, Kolesnik D, Stepanova LI, Golovynska I. Suppression of Tumor Aggression Through Metabolic Reprogramming via Oxamate Targeting LDHA. Int J Mol Sci. 2026; 27.
41. Zhang W, Li Z, Li H, Deng Z, Li S, Wang R, et al. Mutational effects on conformational plasticity redirect the aggregation pathways of intrinsically disordered peptides. Nano Today. 2026; 69: 103044.
42. Ulamec SM, Maya-Martinez R, Byrd EJ, Dewison KM, Xu Y, Willis LF, et al. Single residue modulators of amyloid formation in the N-terminal P1-region of α-synuclein. Nature Communications. 2022; 13: 4986.
43. Senevirathne A, Park JY, Hewawaduge C, Perumalraja K, Lee JH. Eukaryotic expression system complemented with expressivity of Semliki Forest Virus's RdRp and invasiveness of engineered Salmonella demonstrate promising potential for bacteria mediated gene therapy. Biomaterials. 2021; 279: 121226.
44. Leschner S, Weiss S. Salmonella—allies in the fight against cancer. Journal of molecular medicine. 2010; 88: 763-73.
45. Fernandez-Escamilla AM, Rousseau F, Schymkowitz J, Serrano L. Prediction of sequence-dependent and mutational effects on the aggregation of peptides and proteins. Nat Biotechnol. 2004; 22: 1302-6.
46. Riccardi C, Nicoletti I. Analysis of apoptosis by propidium iodide staining and flow cytometry. Nat Protoc. 2006; 1: 1458-61.
47. Hoang NH, Le Thanh T, Sangpueak R, Treekoon J, Saengchan C, Thepbandit W, et al. Chitosan Nanoparticles-Based Ionic Gelation Method: A Promising Candidate for Plant Disease Management. Polymers. 2022; 14: 662.
48. Sivasankar C, Hewawaduge C, Muthuramalingam P, Lee JH. Tumor-targeted delivery of lnc antisense RNA against RCAS1 by live-attenuated tryptophan-auxotrophic Salmonella inhibited 4T1 breast tumors and metastasis in mice. Mol Ther Nucleic Acids. 2023; 34: 102053.
49. Bakhsh M, Senevirathne A, Lee JH. A low-endotoxic Salmonella vector with dual bacterial-host promoter expression of Lawsonia intracellularis antigens elicits protective immunity in a murine model. Vet Res. 2026; 57.
50. Garg VK, Avashthi H, Tiwari A, Jain PA, Ramkete PW, Kayastha AM, et al. MFPPI - Multi FASTA ProtParam Interface. Bioinformation. 2016; 12: 74-7.

51. de Fatima Garcia B, de Barros M, de Souza Rocha T. Bioactive peptides from beans with the potential to decrease the risk of developing noncommunicable chronic diseases. Crit Rev Food Sci Nutr. 2021; 61: 2003-21.
52. Rathore AS, Choudhury S, Arora A, Tijare P, Raghava GPS. ToxinPred 3.0: An improved method for predicting the toxicity of peptides. Comput Biol Med. 2024; 179: 108926.
53. Suri S, Dakshanamurthy S. IntegralVac: A Machine Learning-Based Comprehensive Multivalent Epitope Vaccine Design Method. Vaccines (Basel). 2022; 10.
54. O'Leary NA, Wright MW, Brister JR, Ciufo S, Haddad D, McVeigh R, et al. Reference sequence (RefSeq) database at NCBI: current status, taxonomic expansion, and functional annotation. Nucleic Acids Res. 2016; 44: D733-45.
55. Waterhouse A, Bertoni M, Bienert S, Studer G, Tauriello G, Gumienny R, et al. SWISS-MODEL: homology modelling of protein structures and complexes. Nucleic Acids Res. 2018; 46: W296-W303.
56. Pierce BG, Wiehe K, Hwang H, Kim BH, Vreven T, Weng Z. ZDOCK server: interactive docking prediction of protein-protein complexes and symmetric multimers. Bioinformatics. 2014; 30: 1771-3.
57. Riyaphan J, Pham DC, Leong MK, Weng CF. In Silico Approaches to Identify Polyphenol Compounds as alpha-Glucosidase and alpha-Amylase Inhibitors against Type-II Diabetes. Biomolecules. 2021; 11.
58. Yan Y, Tao H, He J, Huang S-Y. The HDOCK server for integrated protein–protein docking. Nature protocols. 2020; 15: 1829-52.
59. Yan Y, Wen Z, Wang X, Huang SY. Addressing recent docking challenges: A hybrid strategy to integrate template-based and free protein-protein docking. Proteins: Structure, Function, and Bioinformatics. 2017; 85: 497-512.
60. Kielkopf CL, Bauer W, Urbatsch IL. Bradford Assay for Determining Protein Concentration. Cold Spring Harb Protoc. 2020; 2020: 102269.
61. Jiao Z, Jiang J, Meng Y, Wu G, Tang J, Chen T, et al. Immune Cells in the Spleen of Mice Mediate the Inflammatory Response Induced by Mannheimia haemolytica A2 Serotype. Animals (Basel). 2024; 14.
62. Bakhsh M, Senevirathne A, Riaz J, Kwon J, Aganja RP, Cabarles JC, Jr., et al. Bivalent Oral Vaccine Using Attenuated Salmonella Gallinarum Delivering HA and NA-M2e Confers Dual Protection Against H9N2 Avian Influenza and Fowl Typhoid in Chickens. Vaccines (Basel). 2025; 13.
63. Kwon J, Senevirathne A, Lee JH. Multi-route induction of Salmonella-based vaccine delivery elicits protective immunity against FV3-like ranavirus in an ornamental fish model. Fish & Shellfish Immunology. 2025: 111083.